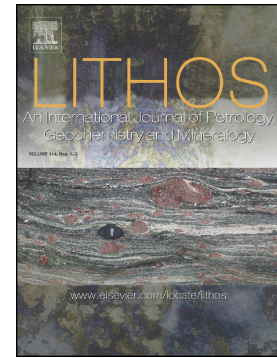


Accepted Manuscript

Tectono-metamorphic evolution of subduction channel serpentinites from South-Central Chile

Gaëlle Plissart, José M. González-Jiménez, Leonardo N.F. Garrido, Vanessa Colás, Julien Berger, Christophe Monnier, Hervé Diot, José Alberto Padrón-Navarta



PII: S0024-4937(19)30123-9
DOI: <https://doi.org/10.1016/j.lithos.2019.03.023>
Reference: LITHOS 5015
To appear in: *LITHOS*
Received date: 10 May 2018
Accepted date: 19 March 2019

Please cite this article as: G. Plissart, J.M. González-Jiménez, L.N.F. Garrido, et al., Tectono-metamorphic evolution of subduction channel serpentinites from South-Central Chile, LITHOS, <https://doi.org/10.1016/j.lithos.2019.03.023>

This is a PDF file of an unedited manuscript that has been accepted for publication. As a service to our customers we are providing this early version of the manuscript. The manuscript will undergo copyediting, typesetting, and review of the resulting proof before it is published in its final form. Please note that during the production process errors may be discovered which could affect the content, and all legal disclaimers that apply to the journal pertain.

Tectono-metamorphic evolution of subduction channel serpentinites from South-Central Chile

Gaëlle Plissart^{a,*} gaille.plissart@uach.cl, José M. González-Jiménez^b,

Leonardo N.F. Garrido^c, Vanessa Colás^d, Julien Berger^e, Christophe

Monnier^f, Hervé Diot^f, José Alberto Padrón-Navarta^g

^aInstituto de Ciencias de la Tierra, Universidad Austral de Chile, Casilla 567, Valdivia, Chile

^bDepartamento de Mineralogía y Petrología, Facultad de Ciencias, Universidad de Granada, Avda. Fuentenueva s/n, 18002, Granada

^cDepartment of Geology and Andean Geothermal Center of Excellence (CEGA), Universidad de Chile, Plaza Ercilla #803, Santiago, Chile

^dInstituto de Geología, Universidad Nacional Autónoma de México, Ciudad Universitaria, 04510 Ciudad de México, México

^eGET, Observatoire Midi-Pyrénées, Université de Paul Sabatier, UMR-CNRS 5563, 14, Avenue Edouard Belin, 31400 Toulouse, France

^fLPG, UMR-CNRS 6112, Université de Nantes, 2 rue de la Houssinière, BP 92208, 44322 Nantes Cedex 3, France

^gGéosciences Montpellier, CNRS & Univ. Montpellier (UMR5243), 34095 Montpellier, France

*Corresponding author.

Abstract

This work provides the first comprehensive petrological and multi-scale structural investigation of a suite of ultramafic bodies and enclosing metasediments from the Late Paleozoic accretionary prism of South-Central Chile. The targeted outcrops are located in the La Cabaña area and are characterized by the presence of three main types of ultramafic rocks: (1) *partially serpentinized massive peridotites*, (2) *antigoritic schistose serpentinites*, and (3) *antigoritic mylonitic serpentinites*. Partially serpentinized massive peridotites and schistose serpentinites recorded a common first hydration event with the formation of Fe²⁺ porous rim in chromites (at ~500°C), followed by static partial transformation of olivine to lizardite (below ~300°C) and formation of rims of Fe³⁺-rich chromite and magnetite around chromites. A second event of serpentinization linked to fluid passage through zones with focused deformation resulted in the partial transformation of partially lizarditized massive peridotites into antigoritic schistose serpentinites (at ~320-400°C). This second event took place within the shallower portion of the serpentinitic subduction channel, near the base of the accretionary prism and was characterized by the formation of tubular folds made up of lenses of olivine-lizardite massive rocks embedded in a matrix of schistose serpentinites. Antigoritic mylonitic serpentinites encountered in the matrix of schistose serpentinites may locally contain metamorphic olivine (i.e., olivine-bearing mylonitic serpentinites), registering higher temperature conditions at medium pressures (~600°C, 11 kbar) that prevailed during the initial immature stage of development of the subduction system. Moreover, some mylonitic serpentinites containing Ti-clinohumite, Ti-chondrodite and metamorphic olivine still record higher pressure conditions (> 15 kbar, i.e., > 50 km depth for ~500°C), which are related with a deformational event taking place when the subduction system had already

cooled. These medium- and high-P mylonitic serpentinites preserved kinematic indicators of burial, whereas their exhumation along the subduction channel towards the shallower schistose serpentinites near the base of the accretionary prism could take place through discrete shear zones possibly aided by large sheath folds. Once incorporated in the accretionary prism (c. 285 Ma ago), the serpentinites shared metamorphism and deformation with the enclosing metasediments. Subvertical shortening related to uplift processes within the accretionary system took place in the stability field of antigorite ($> 300^{\circ}\text{C}$) and, later, a subhorizontal E-W shortening prevailed in more superficial conditions.

Keywords: antigorite; metamorphic olivine; serpentinitic subduction channel; accretionary prism; Chile

1. INTRODUCTION

Serpentinites are rocks containing up to ~13 wt. % H₂O formed by hydration of peridotites in a wide range of temperatures (<650°C) and pressures corresponding to various tectonic settings (Guillot et al. 2015). They have attracted the attention of many geoscientists over the last decades because, when present at the plate interface within subduction zones, they provide insights into mechanisms for the rapid exhumation of deep-seated high-pressure rocks such as blueschists or eclogites (e.g. Cloos and Schreve, 1988; Hermann et al., 2000; Guillot et al., 2001; Agard et al., 2009). This important role of serpentinites resides in their low-density and low-viscosity, which accommodate plastic strain and account for the decoupling of the mantle wedge and the downgoing slab (e.g. Hilairet et al., 2007; Amiguet et al., 2014), allowing return flow of denser rocks. At depths between 30 and 80 km, the subduction interface is made of a 2-10 km thick weak layer (“serpentinic subduction channel”) that can be viewed as a tectonic mélange made of a serpentinitic matrix embedding material mainly derived from the oceanic crust (Guillot et al., 2015). Therefore, the study of subduction channel and associated serpentinites are necessary to understand key processes occurring at convergent plate boundaries (e.g. Guillot and Hattori, 2013; Evans et al., 2013; Deschamps et al., 2013). The existence of the serpentinitic subduction channel is supported by both geophysical imaging (e.g. Hyndmann and Peacock 2003; Hacker et al., 2003) and theoretical computations using numerical approaches (e.g. Schwartz et al., 2001; Gerya et al., 2002; Angiboust et al., 2012).

Despite the importance of studying subduction channels to better understand the evolution of subduction zones, reports of well-preserved structures inside serpentinites associated with this channel are not very abundant. Most of the efforts

have been focused to describe differences in deformation styles between high-P rocks and their host serpentinites (e.g., Monviso in Western Alps, Angiboust et al., 2011). Thus, good examples of subduction-burial and exhumation structures within serpentinites are scarce and poorly known, excepting in the Alps (Erro Tobbio, Hermann et al., 2000; Voltri, Cannà et al. 2016; Zermatt-Saas, Rebay et al., 2012), Japan (Happo ultramafic complex, Nozaka, 2005), and the Betic Cordillera in southern Spain (Cerro del Almirez massif; Padrón-Navarta et al., 2011; Jabaloy-Sánchez et al., 2015). This is due to the fact that usually, later tectono-metamorphic overprints obscured the deep structural relationships.

In the Coastal Cordillera of Chile, small bodies of ultramafic rocks are scattered among metasediments of a fossil accretionary prism, pertaining to a subduction system active during Late Paleozoic-Mesozoic times along the southwest margin of Gondwana (Hervé, 1988; Willner, 2005). While the deformation structures and metamorphic evolution of the metasediments and mafic rocks of this paleo-accretionary prism are relatively well studied (e.g. Willner, 2005; Willner et al., 2005; Kato et al., 2008; Hyppolito et al., 2014), little is known about the petro-structural evolution of the ultramafic rocks associated with them. Previous mineralogical and geochemical analyses by González-Jiménez et al. (2016) of some chromitite and serpentinite samples of La Cabaña area suggest a possible origin of serpentinites related to a subduction channel. More recently, González-Jiménez et al. (2017) have identified humite minerals, including Ti-rich, hydroxyl-dominant chondrodite and clinohumite at La Cabaña, thus confirming for the first time the presence of high-P serpentinites in Chile.

In this paper, we provide the first combined multi-scale structural and petrological analysis from La Cabaña ultramafic rocks in order to better define their

different mineral parageneses and associated microstructures. Additional mineral chemistry and petrological calculations lead us to determine different pressure-temperature-deformation paths (P-T-d) for these rocks that we further integrated in the tectono-metamorphic evolution of the Chilean paleo-subduction system. Our innovative model for the tectono-metamorphic evolution of the ultramafic rocks of South-Central Chile also permits to shed light on the deformation regimes and mechanisms specific to subduction zones.

2. GEOLOGICAL SETTING

The ultramafic rocks of La Cabaña area consist of four large outcrops (namely Centinela Bajo Norte, Centinela Bajo Sur, Lavanderos and Guzmán, Fig. 1) cropping out north of the town of Trovolhue, west of Temuco (Araucania, ~ 38°55'S - 73°30'W, Fig. 1a). They are part of the suite of rocks forming the metamorphic basement of the Chilean Coastal Cordillera (32°-42°S), interpreted as a paleo-accretionary wedge developed at the end of the Paleozoic on the western margin of Gondwana (Hervé, 1988). The Chilean Coastal Cordillera basement is divided into the Eastern and the Western Series (Hervé, 1988) (Fig. 1a), according to the different environments of formation of their rocks (turbiditic meta-greywackes/-pelites *versus* continental metapsammites/-pelites with oceanic lenses), as well as contrasted metamorphic grades (low-pressure (LP) – high-temperature (HT) and high-pressure (HP) – low temperature (LT), respectively). The La Cabaña ultramafic rocks pertain to the Western Series. The rocks of the Western Series experienced HP metamorphism due to basal underplating in the accretionary prism whereas the Eastern Series is a lower-grade unit, which was overprinted locally by HT metamorphism due to the intrusion of Carboniferous continental-arc batholiths

(Willner, 2005) (Fig. 1a). These respective and nearly concomitant PT evolutions permitted to define the Coastal Cordillera as a true fossil-paired metamorphic belt (e.g. Willner, 2005; Willner et al., 2005).

Distinct high-pressure rocks are distributed within the metasedimentary sequence of the Western Series. In the northern part, high-pressure rocks include the Pichilemu blueschists (Fig. 1a), which recorded peak conditions of 9.5-10 kbar and 350-385°C at c. 300 Ma in the subduction channel (Willner, 2005). Additional isolated blocks of garnet-micaschist and amphibolite crop out in the northern part of the Western Series (Punta Sirena area), recording higher peak pressure and temperature conditions (12.5-14 kbar and 540-580°C; Hyppolito et al., 2014, Fig. 1a). These later rocks were interpreted by Hyppolito et al. (2014) as vestiges of the early stages of the subduction system (anticlockwise path characterized by elevated prograde metamorphic gradient and isobaric cooling). Ages for peak pressure conditions estimated for Punta Sirena garnet-micaschists cluster at c. 320 Ma (Willner et al., 2005; Hyppolito et al., 2014) and have been interpreted as the beginning of their exhumation towards the base of the accretionary wedge, with a final incorporation inside this latter at c. 308 Ma (Hyppolito et al., 2014). In the southern part of the Western Series (Fig. 1a), the high-pressure rocks include the Los Pabilos retro-eclogites (13 kbar and 550°C), formed at c. 360 Ma, with a blueschist facies overprint (9 kbar and 400°C) at c. 325 Ma (Kato et al., 2008). Moreover, the entire metasedimentary sequence of the Western Series seems to share "high-pressure" conditions (greenschist-blueschist transitional facies, peak conditions of 7.0–9.3 kbar and 380–420°C, with age estimations at 292–319 Ma), as indicated by high Si contents of phengite in micaschists and high Na contents of amphibole in greenschist metabasites (Willner, 2005; Glodny et al., 2005). This metasedimentary sequence has

been retrogressed to 4-7 kbar and 300-380°C over a period extending 30 to 40 Ma after the metamorphic peak (Willner, 2005). Scattered serpentized ultramafic bodies have also been recognized in the southern part of the Western Series (Fig. 1a) but their origin and metamorphic evolution are still poorly known. Among them, those cropping out in the La Cabaña area are the largest ones (Höfer et al., 2001; González-Jiménez et al., 2014a; 2016; 2017; Romero et al., 2017). They are surrounded by micaschists and mafic schists (Fig. 1b).

3. METHODS

We performed detailed field structural studies on the ultramafic massifs and its enclosing rocks (Fig. 1b). The ultramafic bodies are covered by a thick lateritic soil on which a dense rainforest has developed, which gives little opportunity for direct observation. On the field, the Centinela Bajo Sur, Lavanderos and Loma Guzman bodies show limited outcrops. Therefore, we focused our petro-structural studies on the ultramafic rocks of the Centinela Bajo Norte (Fig. 2). Microscopic observations of ~50 oriented thin sections were undertaken to determine mineralogical assemblages and microstructures. Additional microphotographs were obtained by means of a SEM-EDS, using an EVO MA10 instrument at the Centro de Microscopia de la Universidad Austral de Chile (Valdivia) and operational conditions fixed at 20kV. Deformation events have been also investigated in the enclosing schists and representative photographs can be found in Supplementary Appendix S1.

Contents of major and minor elements were analyzed by WD-XRF on fusion glasses and powder pellets obtained from five representative whole-rock samples (1 dm³) of each one of the lithotypes defined in this study. We used a PANalytical AXIOS instrument at the SERNAGEOMIN (Chile) and the results can be found in

Supplementary Appendix S2. Mg-numbers ($\text{Mg}/(\text{Mg} + \text{Fe}^{2+})$) were calculated considering a Fe^{2+} - Fe^{3+} repartition based on the modal proportion of magnetite (see Supplementary Appendix S6).

X-ray diffraction (XRD) analyses of powder aliquots of the same samples were performed using a Bruker - D2 PHASER diffractometer at the Laboratorio de Superficies Funcionales de la Universidad Austral de Chile (Valdivia), in order to characterize the bulk serpentinite mineralogy and detect the presence of brucite or talc. Results are presented in Supplementary Appendix S3.

Major and minor elements on silicates were measured by electron microprobe analysis (EMPA) using a CAMECA SXFive instrument at the Centre de Microcaractérisation Raimond Castaing (Espace Clément Ader, Toulouse, France). The operational conditions involved a beam current of 20 nA, a beam energy of 15 kV and the counting time was fixed at 10s for peak and background intensity measurements. Natural and synthetic standards were used for external calibration: Na on albite, Al on Al_2O_3 , Si and Ca on wollastonite, K on sanidine, Mn and Ti on MnTiO_3 , Fe on Fe_2O_3 , Mg on MgO, Cr on Cr_2O_3 , Ni on Ni-G5, Zn on sphalerite, F on topaze-TR and Cl on tugtupite. Major and minor elements on spinels were obtained by electron microprobe analysis using a JEOL JXA-8230 at the Centros Científicos y Tecnológicos (Universidad de Barcelona, Spain), with beam current of 20nA and accelerating voltage of 20 kV. The following standards were used for external calibration: periclase for Mg, corundum for Al, diopside for Si, rutile for Ti, metallic V, chromite for Cr, rhodonite for Mn, Fe_2O_3 for Fe, NiO for Ni and sphalerite for Zn. The counting time was fixed at 10s and 5s for peak and background intensity measurement. Data reductions were obtained by application of the PAP program (Pouchou and Pichoir, 1991). Structural formulae of chromite were calculated

assuming stoichiometry following the procedure of Droop (1987). For antigorite, the structural formula has been calculated normalizing to 116 oxygens, considering $Fe_{tot} = Fe^{2+}$ and the ideal formula $M_{3m-3}T_{2m}O_{5m}OH_{4m-6}$, assuming $m = 17$, where m is the number of tetrahedra along a wave (Mellini et al., 1987). Representative microprobe analyses of main minerals can be found in Supplementary Appendix S4.

Serpentine polymorphs have been characterized by micro-Raman spectroscopy (173 analyses) coupled with detailed petrographic observations. Micro-Raman spectroscopy was performed at the Laboratoire de Planétologie et Géodynamique de Nantes, in France, using a LabRam HR Evolution (Horiba) Raman microspectrometer equipped with a laser at an excitation wavelength of 532 nm (power 120 mW) and coupled to an Olympus microscope with X100 objective to focus the laser beam into 1 μ m spot diameter. The spectral resolution was 0.4 cm^{-1} using 1800 lines/mm grating. Acquisition time was 4s with 7 accumulating cycles for shift ranges of 200 to 1000 cm^{-1} (silicate framework domain) and 3400 to 3600 cm^{-1} (OH stretching domain), corresponding to two spectral regions characteristic of serpentine polymorphs (e.g. Schwartz et al., 2013). Description of analyzed spectra is available in Supplementary Appendix S5.

To estimate the pressure-temperature conditions of equilibration of the rocks, pseudosections were performed with *Perple_X* 6.8.4 (Connolly, 2009), using Holland and Powell's thermodynamic database and internally consistent solid solution models for olivine O(HP), orthopyroxene Opx(HP), clinopyroxene Cpx(HP), chlorite Chl(HP), talc T and brucite B (Holland and Powell, 2004) and the solid solution model of Padrón-Navarta et al. (2013) for antigorite Atg(PN), of Powell and Holland (1999) for amphibole GlTrTsPg and of Franzolin et al. (2011) for carbonates oCcm(EF). Calculations of effective chemical compositions during metamorphic peak

are detailed in Supplementary Appendix S6. We tested two methods: 1) by modal proportions, chemical compositions and densities of phases formed during the metamorphic peak, and 2) by bulk rock compositions obtained by WD-XRF and subtraction of phases not involved in the metamorphic peak. Moreover, in both cases, magnetite was subtracted from these compositions in order to compute the pseudosection in the (CaO–) FeO–MgO–Al₂O₃–SiO₂–H₂O (–CO₂) system.

4. STRUCTURAL ANALYSIS

4.1. Ultramafic rocks

The Centinela Bajo Norte ultramafic body displays dispersed outcrops clustering in four main good exposures: Contacto Este (Eastern part), Loma Rurik (Western part), Loma de las Ovejas (Central-Eastern part) and Rio de las Vacas (Northern part) (Figs. 1b and 2). We distinguished three main petrostructural groups characterized by distinctive structures of ductile deformation and degrees of serpentinization (Fig. 2): (1) chromite-bearing and generally coarse-grained *partially serpentinized massive peridotites*, (2) *schistose serpentinites*, and (3) *mylonitic serpentinites*. Moreover, the contact rocks between the ultramafic lithologies and the enclosing micaschists is marked by a blackwall made up of anthophyllite, chloritite and talc schists (Romero et al., 2017).

The ultramafic rocks of the Centinela Bajo Norte body record three main phases of deformation (Figs. 2 and 3), although partially serpentinized massive peridotites show evidence of a previous ductile deformation in the mantle defined by a preferential planar fabric of chromian spinel. The first phase of deformation (D₁) concomitant with serpentinization is an E-W stretching event recorded by elongated lenses and stretching lineation defined by preferred alignment of antigorite needles

and olivine aggregates (L_1) (Fig. 4a, b, c) as well as decametric sheath-like folds (namely F_1 , Fig. 4d, e). When stretching lineation L_1 is visible, the produced fabric is more linear than planar (Fig. 4a). The tubular folds and elongated lenses produced during this deformation stage are made up of competent, chromite-bearing, partially serpentinized massive peridotites, embedded within schistose serpentinites (Fig. 4d, e). Although the orientation of the S_1 foliation associated to this event was affected by the D_2 deformation phase, the geometric relationships between the crenulated S_1 and the competent lenses and folds tend to indicate that S_1 originally wrapped around those lenses (Fig. 4d, e, h). Axes of F_1 and of elongated lenses ($\sim N088/46$) are subparallel to east-plunging stretching lineations ($\sim N076/38$) (Figs. 2 and 3). Opposite senses of shear (asymmetric deformation of lenses) have been observed parallel to the lineation in the same hand-specimen sample, suggesting that a possible shearing has predated the formation of tubular folds. Finally, rare shear bands with top to the east have been observed (Fig. 4b).

The second phase of deformation (D_2) recorded in the serpentinites is a subvertical shortening characterized by recumbent folds that overprints D_1 . This second phase of deformation produced a crenulation of the previous S_1 foliation in the schistose serpentinites, generating a crenulation cleavage S_2 that is frequently accompanied by a lineation of crenulation (L_2) (Fig. 4f, g). This second phase of deformation is particularly observed when S_1 was oriented at low angle relatively to the D_2 shortening axis, near the vertical contacts of the competent lenses formed during D_1 (Fig. 4e, h). In contrast, when S_1 was oriented at high angle relatively to the D_2 shortening axis, the result is a flattening of the previous foliation (S_{1-2}) (Fig. 4d, h). S_{1-2} and S_2 display dips mainly to the east ($\sim N024/35$; Fig. 3), although dispersion in dips to the south and to the north can also be observed. This dispersion is likely due to

the presence of previous E-W elongated competent lenses of partially serpentinized massive peridotites, which would influence the orientation of any new cleavage. In the same way, the bimodal distribution of the crenulation lineations (Fig. 3, D₂, A: ~N084/28 and B: ~N041/22) indicates that one part of the lineation trends is subparallel to the elongated lenses formed during D₁ (eastwards plunges), as is expected alongside the lenses, whereas those distant from the lenses would show orientations reflecting the crenulation event (here plunging to the NE). Two frequent orientations of S₂ crossing at small angle can be observed at the mapping scale (Fig. 2), which we interpret as the two limbs of decametric, inclined, recumbent folds associated to D₂. This is also observed at the outcrop scale with two different orientations of serpentinized relic aligned pyroxenes and with recumbently tightly folded serpentinized pyroxenitic veins, locally isoclinal and with stretched limbs (Fig. 4i).

The third deformation phase (D₃) corresponds to a subhorizontal, SE-NW shortening recorded only in a few outcrops of schistose serpentinites. This phase produced the upright folding of S₂ and development of a subvertical S₃ crenulation cleavage (Fig. 4j). Near the eastern contact with the micaschists, the schistose serpentinites developed a lineation of crenulation L₃ (~N027/13; Fig. 3) that overprints the previous one created during D₂. This crenulation L₃ is particularly visible when L₂ pertains to the east-plunging population, thus resulting in two oblique lineations. The S₃ crenulation cleavage displays high dip and NNE-SSW strikes (~N023/89), which has also been observed in the Centinela Bajo Sur ultramafic body (Figs. 2 and 3). The D₃ phase was also observed as metric anticlines in soap-white schistose serpentinites (Fig. 4k), with S₃ ~N011/71 and L₃ ~N034/28 (Fig. 3). Fragile deformation in ultramafic rocks is recorded by chrysotile and carbonates veins cutting

across all previous structures. However, no coherent information was gained from measured orientations.

4.2. Enclosing schists

The metasedimentary schists (Supplementary Appendix S1) preserved the same deformation structures as observed in ultramafic rocks, except from those of the first deformation phase D_1 . Regional studies indicate that D_1 in the micaschists is only preserved as graphite inclusion patterns inside albite blasts and could be related to processes previous to the basal accretion (i.e. in more superficial conditions) (Duhart et al. 2001), thus differing from the D_1 phase registered in the ultramafic rocks. This D_1 event in micaschists would have been transposed by D_2 , which corresponds to a regional deformation phase observed both in ultramafic rocks and enclosing schists (Fig. 3). The latter show poor evidence of primary sedimentary bedding S_0 and they are dominated by subhorizontal S_2 . The recumbent, tight to isoclinal folding has been nearly completely transposed into the S_2 axial plane foliation. Folding is still observed at places of contrasted competences, such as garnet-quartz or quartzite layers. (Supplementary Appendix S1 a-c). Crenulation cleavage and associated lineation (fold axes and intersection lineations) are also still locally observed. Orientation of S_2 in micaschists ($\sim N021/23$, Fig. 3) is slightly different than in the partially serpentized peridotites: it is also mainly dipping to the east, but it can be subhorizontal and even dipping to the west (Fig. 3). This suggests the presence of N-S striking upright folding that we associated to the D_3 phase. Unlike in ultramafic rocks, the crenulation lineation in micaschists ($\sim N029/13$, Fig. 3) is only plunging to the NE, which could reflect regional D_2 orientation unaffected by previous competent lenses. In micaschists, the D_3 phase formed a subvertical S_3 crenulation cleavage

(Supplementary Appendix S1 d-e) striking NNE-SSW (~N206/88, Fig. 3) and the associated L_3 crenulation is subhorizontal and trends to the NE (~N030/07, Fig. 3). D_3 locally generated L-dominated fabric by the formation of an intersection lineation between S_2 and S_3 . It could also be responsible for the dispersion of S_2 poles (Fig. 3) in zones of more opened folding. Moreover, a fourth deformation event, D_4 , is observed in micaschists; it took place in more brittle conditions and is characterized by localized E-W upright kink folds (Fig. 3) that would result from a subhorizontal N-S shortening.

5. PETROLOGY OF THE ULTRAMAFIC ROCKS

5.1. Microscopic observations

X-ray diffraction was used to detect the presence of fine material unidentified at the microscope (Supplementary Appendix S3). Brucite and talc were not identified, suggesting that, if they exist, their concentration is negligible. Serpentine polymorphs (lizardite, antigorite and chrysotite) were properly identified in the studied serpentinites by their respective spectra (Groppo et al. 2006) obtained using micro-Raman spectroscopy (Supplementary Appendix S5).

5.1.1. Partially serpentinitized massive peridotites (MP)

These rocks are coarse-grained meta-dunites (> 90 vol.% olivine) with variable contents of accessory chromite and pyroxene phantoms (i.e., bastite), which locally grade to meta-harzburgites. Bulk-rock analyses (Supplementary Appendix S2) indicate low SiO_2 (38.04 wt.%), Al_2O_3 (0.03 wt.%), and CaO (0.06 wt.%), high L.O.I. (15.33 wt.%), Cr and Ni contents of 9261 ppm and 3326 ppm, respectively, and a calculated Mg-number of 0.92. The main mineral assemblage is primary olivine +

chromite + lizardite ± chlorite ± magnetite ± late chrysotile (Ol I + Chr + Lz ± Chl ± Mag ± Late Ctl, Fig. 5a). Primary olivine (Ol I, up to 2 mm across) is replaced (20-80%) by a pseudomorphic mesh of lizardite (+ dispersed tiny magnetite) (Fig. 6a), whereas pyroxene (rare in meta-dunites) is completely transformed to bastite. Accessory chromite represents < 2 vol.% of the rock, although it can exceed 10 vol.%, giving rise to dunites with impregnations of chromite and locally schlierens, veins and pods of massive chromitites (Barra et al., 2014; González-Jiménez et al., 2014a; 2016). Chromite preserves homogeneous dark cores surrounded by a porous Fe²⁺-rich chromite rim containing chlorite crystals, locally replaced by a silicate-free homogeneous Fe³⁺-rich chromite, and finally an outer rim of polygonal Cr-magnetite subgrains (Fig. 6b). In some samples, euhedral grains of chromite show an outer halo of chlorite. Finally, late chrysotile (*Late Ctl*) and carbonates veinlets crosscut the mesh structure (Fig. 6a). In the margins of the F₁ folds, the partially serpentinized massive peridotite develops a local schistosity (locally schistose, partially serpentinized massive peridotites – LSch-MP, Fig. 5b) defined by nascent foliation of secondary antigorite overprinting the lizardite mesh (Fig. 6c), which is crenulated in the vertical borders (Fig. 6d).

5.1.2. Schistose Serpentinites (SchS)

The *schistose serpentinites* (*SchS*) are the predominant type of rocks in the Centinela Bajo Norte ultramafic body (Fig. 2) and host the lenses of partially serpentinized massive peridotites. Bulk-rock analyses (Supplementary Appendix S2) indicate low SiO₂ (37.54 wt.%), Al₂O₃ (nil), and CaO (0.01 wt.%), high L.O.I. (14.46 wt.%), Cr and Ni contents of 3508 ppm and 3909 ppm, respectively, and a calculated Mg-number of 0.92. The mineral assemblage observed in the schistose serpentinites

includes primary olivine + chromite + lizardite + overgrown antigorite \pm chrysotile associated to $D_2 \pm$ magnetite \pm chlorite (Ol I + Chr + Lz + Atg \pm Ctl $D_2 \pm$ Mag \pm Chl, Fig. 5c, d). Antigorite first overgrew statically on the mesh lizardite (veinlets and interpenetrating textures) and its growth continued dynamically to give rise to the S_1 foliation (Fig. 6e). It is probable that a L_1 stretching lineation was associated with S_1 but, if so, it has been erased during the D_2 event. Similarly, the orientation of S_1 in these rocks has been affected by D_2 , which generated both foliated (Fol-SchS) and crenulated (Cren-SchS) schistose serpentinites (Fig. 6e). The foliated type formed by transposition of S_2 parallel to a previous S_1 ($S_{1,2}$) whereas the crenulated type resulted from the recumbent crenulation of S_1 , either symmetrically or asymmetrically (Fig. 4h). Limbs of olivine-lizardite ribbons are thinned whereas fractured olivine grains concentrate in thickened hinges (Fig. 6e). Chrysotile veinlets (Ctl D_2) formed in the limbs of the crenulation, subparallel to S_2 (Fig. 6e). Chromite grains in the schistose serpentinites display the same zonation as described in the partially serpentinized massive peridotites. These grains are principally found in the relict mesh textures but also occur in the antigoritic foliation. In the latter case, the magnetite rim generally displays partial inclusions of antigorite (Fig. 5 c-d). Tiny grains of magnetite are only observed in the lizardite mesh texture and are lacking in the antigorite foliation.

5.1.3. Mylonitic serpentinites (MyS, OMyS and TiChu&OMys)

Mylonitic serpentinites are found as small bodies (10-20m wide) dispersed within the groundmass of schistose serpentinites, from which they are distinguished in the field and thin sections by abundant antigorite and the preservation of the L_1 mineral lineation (Fig. 2, Fig. 4a-c). They consist of a matrix of elongated antigorite blades (defining foliation S_1 and pronounced stretching lineation L_1) with accessory

relict chromite and magnetite, and chrysotile associated to D2 (Atg + Chr + Mag ± Ctl D2). This D1 matrix wraps around oriented lenses/ribbons made up of different mineralogical assemblages, which define three subtypes of mylonitic rocks: (1) *mylonitic serpentinites sensu stricto* (MyS), (2) *olivine-bearing mylonitic serpentinites* (OMyS) and, (3) *Ti-clinohumite and Ti-chondrodite olivine-bearing serpentinites* (TiChu&OMyS). Bulk-rock analyses (Supplementary Appendix S2) indicate higher SiO₂ (40.60-44.69 wt.%) and Al₂O₃ (0.11-0.92 wt.%), lower L.O.I. (11.63-11.96 wt.%) and higher calculated Mg-numbers (0.94-0.96) than the massive partially serpentinized peridotites and schistose serpentinites whereas Cr and Ni contents are comparable (3452-3944 ppm and 3173-3218 ppm, respectively). CaO contents are nil except in the olivine-bearing mylonitic serpentinite that contains dolomite (0.38 wt.%). The Ti-clinohumite and Ti-chondrodite sample displays a small enrichment in TiO₂ (0.056 wt.%), V (47 ppm) and Cu (109 ppm).

In the *mylonitic serpentinites ss* (MyS), the lenses consist of interpenetrating antigorite ± chromite ± magnetite (Fig. 5e), with asymmetry indicating a top to the west displacement (Fig. 6f). The contacts between lenses and matrix-oriented antigorite are usually sharp, evidencing the growth of different generations of antigorite and/or a focused strain. In this latter case, the focalization of the deformation during the circulation of fluids triggering the antigorite crystallization could result in the formation of distinct microstructures such as S1-L1 oriented blades and static, randomly distributed blades (Fig 6f). Chromite grains show poorly preserved magmatic cores surrounded by Fe²⁺ and Fe³⁺-rich chromite rims and an outer rim of magnetite, containing inclusions of antigorite (Fig. 6g). Sometimes, magnetite is intergrown with antigorite or forms veinlets (up to 3 mm thick) subparallel or discordant to the foliation (Fig. 5e). Folding during D₂ produced a S₂

crenulation cleavage accompanied by thin chrysotile *Ctl D2* veinlets in the limbs (Cren-MyS, Fig. 5f), which has the effect of locally erasing the interpenetrating antigorite lenses (Fig. 6h).

In the *olivine-bearing mylonitic serpentinites (OMyS)*, embedded as metric zones inside mylonitic serpentinites *ss*, similar lenses of interpenetrating antigorite are observed but they also display lenses and ribbons with olivine II + Atg + Mag ± Chr ± Dol, showing recrystallization tails and curvature of the antigorite blades inside the S1 foliation (Fig. 5g). The olivine II forms poikiloblasts hosting needles of antigorite ± magnetite (Fig. 6i) or elongated grains, up to 1 mm, lacking internal solid-state deformation and with frequent magnetite inclusions (Fig. 6j, k), which is characteristic of metamorphic olivine (Ol II). Dolomite displays tabular elongated untwinned grains (Fig. 6j) or poikiloblasts with sharp contacts with antigorite needles and magnetite inclusions (Fig. 6i). Antigorite is hosted as inclusions in olivine, dolomite and magnetite. Olivine and dolomite have been found as inclusions in magnetite (Fig. 6m). Chromite grains (Fig. 6l) display similar features as in mylonitic serpentinites, but with a very well-developed outer magnetite rim containing large antigorite inclusions. Late lizardite statically replaces olivine borders.

The *Ti-clinohumite and Ti-chondrodite olivine-bearing serpentinites (TiChu&OMyS)* were found nearby diopside veins and exhibit the same petrostructural features as the olivine-bearing serpentinites, excepting for the lack of dolomite and the presence of Ti-clinohumite and rare Ti-humites and Ti-chondrodite (Fig. 5h). The Ti-clinohumite and Ti-humite are usually intergrown with olivine II, generally found at their rims, whereas Ti-chondrodite occurs as fine lamellae inside Ti-clinohumite (Fig. 6n, see also González-Jiménez et al., 2017). Antigorite included

in olivine and Ti-clinohumite is clear under reflected light microscope whereas that forming the matrix may exhibit a characteristic pale yellow/brown pleochroism due to the presence of several inclusions of retrograde lizardite-chrysotile laths (Fig. 6o). Like the mylonitic serpentinites, the S_1 antigorite was highly bended during the D_2 deformation phase, producing the S_2 crenulation cleavage and local recrystallization of antigorite (Fig. 5h) whereas chrysotile veinlets (*Ctl* D_2) crystallized in the crenulation limbs, subparallel to the crenulation D_2 axial plane (Fig. 6o).

5.2. Mineral chemistry

About 350 electron microprobe analyses were carried out on rock-forming minerals (silicates, chromite, magnetite and carbonates) from polished sections from the different lithotypes identified in this study. Representative analyses are given in Supplementary Appendix S4.

5.2.1 Silicates

Relict olivine ($n = 79$) preserved in partly serpentinized peridotites and schistose serpentinites is forsterite ($Fo = 89-93$, typical of mantle olivine compositions, Scambelluri et al. 1991) with NiO contents of 0.28-0.43 wt.% and low MnO contents (0.10-0.26 wt.%) without core to rim zoning (Fig. 7a). In contrast, secondary olivine (i.e., Ol II; $n = 60$) identified in the mylonitic serpentinites is overall richer in MgO ($Fo = 90-97$, probably controlled by bulk rock composition), NiO (0.32-0.54 wt.%) and MnO (0.10-0.66 wt.%) (Fig. 7a; Supplementary Appendix S4a). This secondary olivine displays core-to-rim zoning characterized by an increase of the Fo content (Fig. 7b; Supplementary Appendix S4a).

Mesh lizardite ($n = 10$) in partly serpentinized massive peridotites yields variable MgO (36.27-40.75 wt.%), low SiO₂ (30.60-39.27 wt.%), high total FeO (4.42-8.12 wt.%) and low total major element contents (79.97-83.12 wt.%), with very little amounts of Al₂O₃ (nil to 0.03 wt.%, except for one analysis at 0.8 wt.%). (Supplementary Appendix S4b). In contrast, mesh lizardite ($n = 2$) in schistose serpentinites and static haloes around secondary olivine is almost pure with MgO = 39.27-40.22 wt.%, SiO₂ = 42.77-43.43 wt.%, low total FeO = 1.35-3.17 wt.% and normal total major element contents (85.26 -85.24 wt.%) (Supplementary Appendix S4b).

Chrysotile in veinlets associated to the S₂ crenulation (*Ctl D2*) displays MgO = 37.54 wt.%, SiO₂ = 42.43 wt.%, total FeO = 3.12 wt.% and normal total major element contents (83.28 wt.%).

Antigorite ($n = 57$; Supplementary Appendix S4b) displays mean MgO of 39.59 wt.%, high SiO₂ (mean of 44.10 wt.%), low total FeO (mean of 2.12 wt.%), mean total major element contents of 86.23 wt.% and variable amounts of Al₂O₃ (mean of 0.94 wt.%). Al contents are particularly high in the antigorite from the low-schistose partially serpentinized massive peridotites (0.97-3.03 apfu; Fig. 7c). Overall, an increase of the Al contents can be observed in antigorite blades from schistose serpentinites (0.31-0.60 apfu) to mylonitic serpentinites (0.10-1.19 apfu) and to Ti-clinohumite and Ti-chondrodite olivine-bearing mylonitic serpentinites (0.35-1.55) (Fig. 7c), except for the antigorite from olivine-bearing mylonitic serpentinites, which shows low Al contents (0.03-0.43, Fig. 7c). We assumed that Fe³⁺ in antigorite is very low as its Mg# considering $Fe^{2+} = Fe_{tot}$ (OMyS: 0.98-0.99; TiChu&OMyS: 0.96-0.97)

approaches the value in equilibrium with corresponding metamorphic olivine (OMyS: 0.96-0.97; TiChu&OMyS: 0.90-0.92) (Evans et al., 2012).

González-Jiménez et al. (2017) have recently reported the composition of Ti-clinohumite and Ti-chondrodite identified in mylonitic serpentinite (Supplementary Appendix S4c). The analyzed grains exhibit stoichiometry close to theoretical formula with the ratios $2\text{Si}/[2n/(2n+1) * M_{\text{Ti}}]$ ratios ($n = 4, 3$ and 2 for clinohumite, humite and chondrodite, respectively; Jones et al., 1969) approaching 1 (1.014-1.058; 1.003-1.005; 1.017-1.047, respectively). Fluorine contents are overall very low or below detection limits (< 0.22 wt.%) in Ti-clinohumite and Ti-humite and slightly higher in Ti-chondrodite (up to 0.587 wt.%) (Supplementary Appendix S4c). TiO_2 contents are high (Chu: 3.5–5.2 wt.%; Hu: 6.5 wt.%; Chn: 7.8–9.3 wt.%) and vary within the following ranges of $x = 0.34$ – 0.43 (TiChu), 0.42 – 0.43 (Hu) and 0.36 – 0.43 (TiChn) in the general formula $n\text{M}_2\text{SiO}_4 \text{M}_{1-x}(\text{OH},\text{F})_{2-2x} \text{Ti}_x\text{O}_{2x}$ (Fig. 7d), thus below the Ti-saturation limit of $x = 0.5$ (Jones et al., 1969). MnO contents show quite elevated ranges: 0.52-0.70 wt.% in Chu, 0.63-0.65 wt.% in Hu and 0.61-0.70 wt.% in Chn.

5.2.2 Chromite and magnetite

Chromite ($n = 28$) from all the different lithotypes exhibits homogeneous dark cores with composition varying from the high-Al to high-Cr types [$\text{Cr}\# = \text{Cr}/(\text{Cr} + \text{Al})$ atomic ratio = 0.57-0.71] and variable Mg# [$\text{Mg}/(\text{Mg} + \text{Fe}^{2+})$ atomic ratio = 0.34-0.63] (Fig. 8a). These cores are surrounded by an internal rim of Fe^{2+} -rich (up to 25.29 wt.% FeO) porous chromite ($n = 13$) with higher Cr# (0.85-0.99) and lower Mg# (0.17-0.31), and an outer homogeneous rim of Fe^{3+} -rich chromite (i.e., ferrian chromite; $n = 20$) with 16.39-45.79 wt.% Fe_2O_3 , Cr# = 0.75-0.99 and Mg# = 0.18-0.40 (Fig. 8a, b). Chemistry of the chromite cores and their surrounding rims is

relatively constant in samples of the same lithotype but strongly varies among lithotypes (Fig. 8; Supplementary Appendix S4d). Magnetite overgrowing on the Fe³⁺-rich rim and magnetite individual grains (n = 40) have Cr# = 0.84-1.00 and Mg# = 0.03-0.24 (Fig. 8). A comparison of TiO₂, MnO, ZnO and NiO contents in chromite core, rims and magnetite from the different lithotypes can be found in Supplementary Appendix S4d.

5.2.3 Dolomite

Dolomite (Supplementary Appendix S4e) displays consistent and nearly pure composition, with an average of Ca₄₉Mg₅₀Fe_{0.6}Mn_{0.4}.

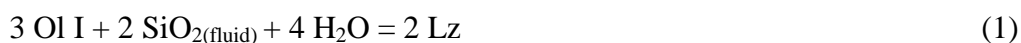
6. DISCUSSION

6.1 Metamorphic conditions

6.1.1 Retrograde serpentinization of mantle peridotites

Partially serpentinized massive peridotites and schistose serpentinites exhibit whole rock Mg-numbers varying between 0.91 and 0.93 (Supplementary Appendix S2), which is typical of abyssal or mantle wedge serpentinized mantle peridotites (Deschamps et al. 2013). Olivine in rocks with scarce pyroxene phantoms (i.e., bastite) displays Fo contents of 91-93 typical of mantle dunites (Fig. 8a; Supplementary Appendix S4a), whereas rocks with higher proportion of bastite yield lower Fo contents (89-90) as is typical for mantle harzburgites. These rocks preserve a first retrograde event of serpentinization marked by the static replacement (80 vol.% modal) of primary olivine by mesh lizardite (Fig. 6a, c, e) at temperatures < 300°C (Evans, 2004). The lack of brucite in these samples suggests that olivine could

transform to lizardite without brucite formation via its interaction with silica-rich fluids (Frost and Beard, 2007):



or that brucite eventually formed during lizarditization was removed from the system by reaction with these silica-rich fluids through the following reactions (Frost and Beard, 2007):



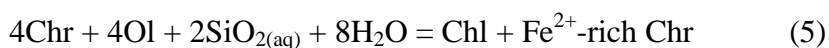
followed by



The SiO_2 -rich fluids could derive from the dehydration of metasediments from the subducting slab (Manning, 1997) and/or complementary from the hydration of pyroxenes present in the meta-dunites or meta-harzburgites such as suggested by Frost and Beard (2007) and Evans et al. (2013):

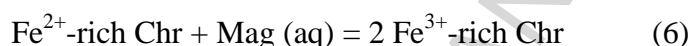


This first stage of retrograde alteration of the mantle peridotites is also recorded in these rocks by the formation of porous Fe^{2+} -rich inner rims containing chlorite (Fig. 9ii) in accessory chromite grains. These rims may have formed by the retrograde reaction between chromite and host olivine possibly aided by the infiltration of reducing fluids with relatively high SiO_2 (aq) in the peridotites at 510–560 °C (González-Jiménez et al., 2016):



These temperatures are higher than the estimations for the lizarditization ($< 300^{\circ}\text{C}$) observed in the partially serpentinized massive peridotites and schistose serpentinites. Thus, the formation of the Fe^{2+} porous chromite rim indeed predates the lizarditization event recorded in these rocks (Fig. 9), otherwise it would have erased the low T minerals.

The observation of homogeneous rims of Fe^{3+} -rich chromite overgrowing on, or replacing, the pre-existing Fe^{2+} -rich porous chromite rims suggests a second event of alteration related with the circulation of oxidizing fluids carrying magnetite component. The formation of this rim can be explained by the following reaction (Gervilla et al., 2012):



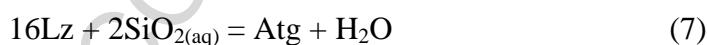
This second retrograde alteration could be concomitant with the first lizarditization event recorded in partially serpentinized massive peridotites and schistose serpentinites (Fig. 9iii). Silica incorporated by the serpentinizing fluids could have enhanced the alteration of chromite (Colás et al., 2017) while the excess of Fe_{total} in the structure of the secondary Fe^{3+} rich chromite may explain the formation of outer magnetite rims surrounding these chromite grains.

6.1.2 Prograde antigoritization of serpentinites

A second event of serpentinization is related to the formation of prograde antigorite as: (i) static blades overgrowths on the mesh lizardite at the margins of the F_1 folded partially serpentinized massive peridotites (Fig. 6c, d) and in the schistose serpentinites (Fig. 6e); (ii) dynamic recrystallization of oriented blades (i.e., foliation S_1) in the schistose serpentinites ($\sim 50\%$ modal antigorite) (Fig. 6e); (iii) deformed

lenses of static interpenetrating antigorite in the mylonitic serpentinites (Fig. 6f); and (iv) L₁-S₁ mylonitic fabric in the mylonitic serpentinites (100% modal antigorite, Fig. 6f) containing or not metamorphic olivine and/or Ti-clinohumite and Ti-chondrodite (Fig. 6i, j, o). These differences in the antigorite microstructures suggest that the deformation associated to the D1 phase was localized, and that the fluid infiltration producing antigorite (re-)crystallization very likely took place at different temperatures.

In the margins of the F₁ folded lenses of *partially serpentinitized massive peridotites* and in the *schistose serpentinites* wrapping these folded lenses, the coexistence of lizardite and antigorite restricts the temperature of hydration at 320-390°C (Schwartz et al., 2013) (Fig. 9iv, Fig. 10a). The observation that, in these rocks, antigorite has higher SiO₂ contents (40.4-44.5 wt. %) than the coexisting lizardite (30.6-42.77 wt. %) suggests that the transformation of lizardite to antigorite was very likely promoted by the progressive infiltration of SiO₂-rich fluids, probably released by the subducting slab (Manning, 1997). This transformation of lizardite to antigorite in presence of silica-rich fluids could be explained by the following reaction (Evans, 2004; Frost and Beard, 2007):



Noteworthy antigorite in the margins of the F₁ folded lenses of partially serpentinitized massive peridotites displays higher Al₂O₃ and lower SiO₂ than antigorite found in the nearby schistose serpentinites (Fig. 7c), reflecting the analysis of a lizardite/antigorite intergrowth and thus an incomplete antigoritization of lizardite in these zones.

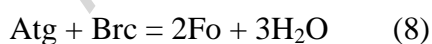
On the other hand, the complete antigoritization observed in *mylonitic serpentinites* (Fig. 9v) could reflect higher fluid/rock ratios during hydration by silica-rich fluids or higher temperature-pressure conditions of equilibration than in partly serpentinitized massive peridotites and schistose serpentinites. Indeed, the relatively high Al contents in the antigorite (up to 1.186 apfu; Fig. 7c) suggest serpentinitization at relatively higher temperatures (390-460°C; Schwartz et al., 2013), although below the stability field of metamorphic olivine. Consistently, the pseudosection performed in the FMASH system for a representative sample of olivine-free mylonitic serpentinite (Fig. 10b; sample CA-15-5; Supplementary Appendix S6 for calculations details) predicts the existence of a pentavariant field consisting of the assemblage antigorite + talc (91 vol.% + 9 vol.% respectively) stable at temperatures below ~550°C at 10 kbar (the upper limit corresponding to the production of metamorphic olivine). The fact that we have not detected talc neither in thin section nor by XRD bulk-rock analysis of these samples might reflect differences between the pure (Si = 34 apfu, Mg = 48 apfu) and measured (Si_{mean} = 34.4 apfu; (Mg + Fe + Mn + Ni)_{mean} = 46 apfu) antigorite.

6.1.3 Partial dehydration of serpentinites

Mylonitic serpentinites containing olivine (i.e., OMyS and TiChu&OMyS) are characterized by olivine in textural equilibrium with antigorite, magnetite and locally dolomite and humite minerals (Fig. 6i-o). This suggests a metamorphic origin of this second generation of olivine (Ol II), which clearly attests an event of partial dehydration (e.g. Li et al., 2004; Nagaya et al., 2014). Moreover, this secondary olivine (Ol II) is characterized by high MnO contents (Fig. 7b), as is typical of metamorphic olivine described in serpentinites that have experienced partial

dehydration elsewhere (Scambelluri et al., 1991; Trommsdorff et al., 1998; Li et al., 2004; López Sánchez-Vizcaíno et al., 2005; Padrón-Navarta et al., 2011; de Hoog et al., 2014; Nagaya et al., 2014). The deformed Atg + Mag + Ol (+ Dol) lenses and the shape preferred orientation of olivine, magnetite and dolomite grains inside the ribbons (Fig. 6i, j) indicate that this event of partial dehydration was associated with the D1 deformation phase.

In the mylonitic serpentinites consisting of Ol II + Atg + Mag ± Dol ± Chr, olivine is in textural equilibrium with antigorite, magnetite and locally dolomite (Fig. 6i, j). The static lenses of antigorite and magnetite strings seem to correspond to places for the preferential nucleation of the new assemblage Ol II + Atg + Mag ± Dol. Moreover, the fact that crystal-shaped dolomite is included in magnetite while displaying textural equilibrium with the other minerals (Fig. 6m) clearly indicates that the carbonate was part of the metamorphic peak assemblage. A pseudosection computed for the dolomite-free assemblage (Ol II + Atg + Mag; Fig. 10c; sample CA-15-3a; Supplementary Appendix S6 for calculations details) in the FMASH system predicts the existence of a tetravariant field with coexisting olivine and antigorite between 450°C and 600°C at 10 kbar. As shown in Figure 10c, the formation of the metamorphic olivine at expenses of antigorite should take place according to this reaction:



However, the mylonitic serpentinite used for pseudosection computations lacks of brucite as attested by the bulk-rock XRD analysis (Supplementary Appendix S3), suggesting either that these serpentinites derived from a rock already lacking brucite, or that brucite was completely consumed during reaction 8, or that its presence in the

pseudosection derives from uncertainties inherent to calculations. Similarly, a pseudosection performed for the dolomite-rich domain of this mylonitic serpentinite (Ol II + Atg + Mag + Dol; Fig. 10d; CA-15-3b; Supplementary Appendix S6 for calculations details) in the CFMASHC system predicts a more restricted stability field for the assemblage olivine + antigorite + dolomite, thus better constraining the metamorphic peak of this rock at 11 kbar also at 600 °C. These later P-T conditions were estimated considering $X_{CO_2} [nCO_2/(nH_2O+nCO_2)] = 0.02$, which produced the best possible fit between the Ol + Atg + Dol field and the isopleths of observed volume proportions of olivine (21.5%), antigorite (76.9%) and dolomite (1.6%) and the measured XAl in antigorite (0.053) of the studied rock. Such X_{CO_2} value is lower than those estimated for fluids associated to high-P ophicarbonate assemblage (Scambelluri et al. 2016). The results of the above calculations for dolomite-free (Fig. 10c) and dolomite-bearing (Fig. 10d) domains in the same sample are very close to each other, thus the superposition of the stability fields obtained from both pseudosections yields ~600°C at 11 kbar as the metamorphic peak. The slight differences observed between the two assemblages in the same rock may be attributed to uncertainties inherited to pseudosection calculations as well as scattered presence of dolomite, which reflects the heterogeneous circulation of CO₂ and Ca-bearing-fluids.

On the other hand, a third type of mylonitic serpentinites identified in the La Cabaña ultramafic massif contains Ti-clinohumite, Ti-humite and Ti-chondrodite in equilibrium with olivine, magnetite and antigorite (Fig. 7n, o). González-Jiménez et al. (2017) estimated a metamorphic peak for these rocks at ca. 1.5–2.5 GPa and 450–650 °C on the basis of the P-T grid constructed by Shen et al. (2015) for F-free assemblages and Ti-poor rocks. The results of this approach are fully consistent with

(1) the new bulk-rock data provided in this study showing that these rocks have relatively low TiO₂ contents (0.056 wt.%; Supplementary Appendix S2), overlapping those reported for other HP serpentinites containing this mineral assemblage (e.g., Scambelluri et al., 2001; Shen et al., 2015), and (2) the very low F contents (< 0.22 wt.%) in Ti-clinohumite (Supplementary Appendix S4c).

6.1.4 Final retrogression of the low, medium and high-pressure serpentinites

An event of antigorite recrystallization associated with the D₂ deformation phase is recorded in all the lithotypes, i.e., partially serpentinitized massive peridotites, schistose serpentinites, mylonitic serpentinites and (Ti-clinohumite +) olivine-bearing mylonitic serpentinites. During this second phase of deformation D₂, the S₁ antigorite blades were crenulated or recrystallized giving rise to the S₂ antigorite crenulation cleavages (Fig. 6d, e, h, o). The fact that antigorite recrystallized suggests that the D₂ phase took place still within the stability field of antigorite at ~320-460°C (Schwartz et al., 2013). Moreover, the *Ctl* D₂ veinlets filling the voids in the limbs of the D₂ crenulation (Fig. 6d, e, o) suggest that the formation of chrysotile was also linked to this deformation phase. This observation confirms the results of experiments obtained by Evans (2004) who showed that the stability field of chrysotile in serpentinites may be controlled by a high fluid/rock ratio rather than solely temperature and/or pressure.

The latest events of hydration are marked by (i) static lizarditization of metamorphic olivine and (ii) a second generation of veins of chrysotile (*Late Ctl*) and carbonates cutting the D₂ structures in all lithological types. This observation suggests that this late infiltration of fluids took place once D₂ deformation ceased.

6.2 Tectono-metamorphic evolution

6.2.1 Pre-subduction retrograde stage

Bulk-rock geochemical data on partially serpentinized massive peridotites and schistose serpentinites of La Cabaña display patterns similar to those of mantle wedge serpentinites with dunitic and harzburgitic protoliths (González-Jiménez et al., 2016; TiO_2 contents < 0.015 wt% anhydrous, Supplementary Appendix S2). This is consistent with the composition of the primary cores of accessory chromite in these rocks characterized by high Cr# (0.57-0.71) and Mg# of 0.34-0.63, which overlap the compositional field of accessory Cr-spinel of sub-arc peridotites (e.g. Barnes et al., 2013) (Fig. 8a). This is also consistent with the presence of chromitites hosted in these types of rocks, which were formed within the protolithic dunites (representing pathways for melt extraction) in the back-arc mantle above a subduction zone (González-Jiménez et al., 2014a). The high Fo contents (between 89-90 and 91-93) in the massive partially serpentinized peridotites and the schistose serpentinites (Fig. 7a) are also consistent with a strongly depleted nature of the peridotite protolith, as high rates of hydrous partial melting (> 25%) are necessary to promote formation of chromitites and host dunites in the suprasubduction mantle (González-Jiménez et al., 2014b). The existence of a small back-arc basin developed in the rear of an intra-oceanic island arc (Fig. 11a) has already been suggested for the southern part of the Central Chilean paleo-subduction system on the basis of the following evidences: (1) presence of volcanic massive sulfides deposits, which are typical in back-arc settings (Alfaro and Collao, 1990), (2) subduction-related basalts with faint Nb anomalies (Orellana et al., 2015), and (3) a population of zircons in metasediments that yield an age of c. 380 Ma, very unusual for detrital zircons from metasediments of the

paleoprism, which could represent remnants of a Devonian volcanic arc (Romero et al., 2017).

The retrograde static events of chromite alteration and lizarditization (down to ~ 300°C), now well preserved in partly serpentinized massive peridotites and schistose serpentinites, can be linked with an event of hydration within the seafloor of the slow spreading center in the back-arc basin and/or following the closure of this small back-arc basin leading to progressive hydration of the hanging mantle by slab-derived fluids (Fig. 11b).

6.2.2 Progressive subduction and exhumation in the subduction channel

Partly serpentinized massive peridotites and schistose serpentinites record a second serpentinization event at 320-390°C with the superimposition of antigorite on previous lizardite (Fig. 6c, d, e). The growth of non-oriented blades overprinting the lizardite mesh suggests that fluid percolation was first static whereas antigorite S1 foliation indicates that, subsequently, this transformation took place during the D1 deformation phase, localizing the deformation and differentiating low viscosity zones (Fig. 9iv). This is consistent with the observed tubular folds between schistose serpentinites and competent, partly serpentinized massive peridotites lenses. Such structures (Fig. 12a) suggest a combination of vertical shortening and subhorizontal simple shearing, usually related with processes operating near or within the subduction channel (Cloos and Schreve, 1988; Angiboust et al. 2012). This suggests that the previously statically hydrated protolith was displaced to higher depths, near the subduction channel (Fig. 11c), which could be related to a progressive thickening of the accretionary prism and/or to corner mantle flow allowing burial of mantle wedge peridotites. However, the widespread preservation of primary olivine and

lizardite indicates that these rocks never underwent a significant burial but rather remained near the shallow portions of the serpentinitic subduction channel. In the above scenario, relatively hot and silica-rich fluids may have infiltrated the already lizarditized mantle wedge peridotites while producing partial antigoritization through zones with focused strain. Once formed, these zones could in turn have allowed further focusing of deformation and channeling of incoming fluids, enhancing the formation of a weaker matrix of schistose serpentinites whereas preserving panels of portions of partly lizarditized mantle peridotites amidst further fluid infiltration and antigoritization (Fig. 12b). This is consistent with the fact that antigorite blades are located at the margins of the lenses of partially serpentinitized massive peridotite but not in their innermost zones (Fig. 6c, d). Thus, both rocks followed a similar subduction PT path close to the deeper parts of the accretionary prism (Fig. 11c).

As noted above, mylonitic serpentinites (MyS, OMyS, TiChu&OMyS) record higher temperature conditions, thus suggesting a different evolution. Because mylonitic serpentinites *sensu stricto* and olivine-bearing mylonitic serpentinites crop out together on the field and display similar L1 stretching lineation evidenced by antigorite blades and shape preferred orientation of olivine and magnetite in ribbons (Fig. 4a, b, c), they could have suffered a concomitant, non-coaxial D1 strain within the serpentinitic subduction channel. Moreover, kinematics indicators associated to D1 show a general vergence to the west (Fig. 6f) compatible with burial, which would be in agreement with the prograde Fo zoning preserved in metamorphic olivine (Fig. 7b; Fig. 10c, d). We thus suggest that both rocks equilibrated at similar PT conditions (estimations of $\sim 11\text{kbar} - 600^\circ\text{C}$ considering the uncertainties inherent to pseudosection calculations) and that the presence or absence of metamorphic olivine could reflect local variations in their bulk compositions. This is consistent with the

geometry of the pseudosections (Fig. 10b, c, d), which display the formation of metamorphic olivine at lower temperatures for OMyS (~450°C) than for MyS (~575°C) for a same pressure of 11 kbar. We thus consider that these rocks reached ~40 km depth inside the serpentinitic subduction channel and recorded a hot, anti-clockwise PT pathway, when the subduction system was still thermally immature (Fig. 11b, c). This evolution would be similar to the counterclockwise PT path recorded by nearby garnet-bearing amphibolites (12kbar - 610°C; Moral et al., 2018) or by other rocks inside the Chilean paleo-prism (Punta Sirena, Hyppolito et al. 2014; Los Pabilos, Kato et al. 2008). The (olivine-bearing) mylonitic serpentinites were probably located at the boundary between the hanging wall and the nascent subduction channel because they were not dragged within the channel, but rather remained stagnant at the same depth while undergoing isobaric cooling (Fig. 11c).

As noted above, the Ti-clinohumite and Ti-chondrodite olivine-bearing mylonitic serpentinites would have registered higher pressure conditions than the other serpentinites of La Cabaña (field of 450°C < T < 650°C and 15 kbar < P < 26 kbar; González-Jiménez et al., 2017). The Fo zoning in olivine suggests that these rocks preserved a prograde path (Fig. 7b) and the abundance of antigorite indicates an incomplete dehydration of these rocks, which probably entered the Atg + Ol + Ti-Chu + Ti-Chn field along a cool, clockwise pathway. This subduction event of the serpentinites down to depths of 60 km should have been taken place when the subduction system was already thermally mature (Fig. 11c).

Rare senses of shear with top-to-the-east (opposite to the one of subduction) are preserved in mylonitic serpentinites (Fig. 4b). This observation suggests that, before to be incorporated into shallow schistose serpentinites, medium and high-P

rocks (MyS, OMyS and TiChu&OMyS) were exhumed along discrete shear zones inside the subduction channel, similarly to reported for the Erro Tobio (Voltri) unit in the Italian Alps (Hermann et al., 2000). In addition, sheath-like folds could also take part in the exhumation, with the medium- and high-pressure rocks preserved in their “head” (Fig. 12a). This suggests that the La Cabaña massif corresponds to a shallow portion of a serpentinitic channel derived from mantle wedge (MP, SchS) inside which were emplaced rare, exotic rocks registering other PT conditions (MyS, OMyS, TiChu&OMyS). Subduction channels with serpentinites exhibiting heterogeneous metamorphic evolutions have also been reported by Federico et al. (2007) in the Voltri massif, Guillot et al. (2009), Blanco-Quintero et al. (2011) in Cuba and Bebout and Penniston Dorland (2016).

6.2.3 Incorporation of the ultramafic rocks into the accretionary prism and subsequent co-evolution

As noted above, the different lithotypes from the La Cabaña ultramafic rocks share the D_2 crenulation also characteristic of the enclosing micaschists (Fig. 3). This suggests that the different ultramafic lithotypes were already juxtaposed before their incorporation inside the metasediments from the paleo-accretionary prism (Fig. 11d). This incorporation of the ultramafic bodies inside the prism probably followed the style of D_1 initiated in the shallow portions of the serpentinitic subduction channel. Indeed, similar sheath-like folds have been described in metasedimentary and mafic rocks in other parts of Chile (Bahia Mansa Metamorphic Complex, Maule Valley), which resulted from strain acting at the base of the accretionary prism (Duhart et al., 2001; Glodny et al., 2005; Richter et al., 2007; Plissart et al., 2015). The observation that the D_1 fabric is preserved both in the serpentinites and the enclosing metasedimentary schists suggests that there was a continuum in the style of

deformation from the shallow portions of the serpentinitic subduction channel to the base of the accretionary prism (Fig. 12a). Although this tectonic mixing was not complete (no metasediments have been encountered inside ultramafic rocks), there was development of a metasomatic reaction zone between the more rigid ultramafic body and the host metasediments (i.e., black-wall; Höfer et al., 2001). Metasomatic zircons date the formation of this black-wall at 283.4 ± 7 Ma (Romero et al., 2017), and therefore the incorporation of the ultramafic rocks inside the base of the accretionary prism (Fig. 11e). According to Höfer et al (2001), the assemblage of tremolite + antigorite constrains the temperature of formation of this black-wall at 520-550°C. However, these conditions were obtained by comparing a stability diagram constructed for an average serpentinite and not for the composition of the observed metasomatic rock, and this bimineralic, high variance assemblage is probably stable over a wide PT range. Moreover, these conditions contradict with the preservation of mesh lizardite in partly serpentinitized peridotites and the lack of widespread metamorphic olivine in the La Cabaña rocks. Rather, our petrological observations indicate that the temperatures did not exceed $\sim 400^\circ\text{C}$ (Fig. 11e), consistent with the PT conditions estimated for mixed metasediments-mafic rocks from the base of this accretionary prism (380–420°C and 7.0–9.3 kbar; Willner, 2005; Glodny et al., 2005).

Once incorporated in the accretionary prism, the subvertical shortening D_2 event (Fig. 12a), characterized by crenulation of S_1 and formation of S_2 presently dipping mainly to the east (Fig. 4f-i), affected the whole ultramafic rock suite as well as the enclosing metasediments. Glodny et al. (2005) interpreted this deformation event, based on the tectono-metamorphic evolution of micaschists from the Valdivia area (40°S) and analogue experiments, as an erosion-dominated unroofing with uplift

governed by the ongoing underplating. Although the pressure is not constrained for D_2 , the recrystallization of antigorite in the S_2 cleavages (Fig. 7e, h, o) suggests that it prevailed at temperatures higher than 300°C , which could fit the conditions of exhumation and retrogression registered in the metasediments of the Western Series ($300\text{-}380^\circ\text{C}$; 4-7 kbar) (Willner, 2005) (Fig. 11e). Later, the E-W subhorizontal shortening D_3 generated N-S upright folds and S_3 foliation (Fig. 3; Fig. 12a). This deformation phase might be related to mechanical processes linked to frontal accretion once the previously juxtaposed ultramafic bodies and enclosing rocks had already begun their vertical exhumation inside the accretionary prism (Fig. 12a). Finally, D_4 , mainly observed in the micaschists, took place at the ductile-fragile transition as showed by kink bands, evidencing more superficial depths within the prism.

CONCLUSIONS

The ultramafic rocks from the La Cabaña area correspond to a portion of a subduction channel developed during the formation and evolution of the Central Chilean paleo-subduction zone in the Paleozoic. Partially serpentinized massive peridotites recorded the evolution of the uppermost part of the mantle corner before to be captured by the subduction channel. A first retrograde static event ($< 300^\circ\text{C}$) probably occurred after the closure of an incipient back-arc basin, leading to static hydration of the hanging wall. Subsequently, the accretionary prism thickened and the partially serpentinized massive peridotites moved near its base where a second, prograde hydration event occurred in the stability field of antigorite ($\sim 320\text{-}400^\circ\text{C}$). At this stage fluid infiltration was focused on zones with focused high strain, which now correspond to schistose serpentinites wrapping the partially serpentinized massive

peridotites. The strong rheological contrast between both domains and the deformation prevailing near the base of the prism generated the tubular-like folds and lenses of partially serpentinized massive peridotites embedded in schistose serpentinites. Olivine-free and olivine-bearing mylonitic serpentinites probably formed in a thermally immature subduction system (600°C- 11 kbar; ~40km). By contrast, Ti-clinohumite and Ti-chondrodite olivine-bearing metamorphic serpentinites would have formed deeper (450°C < T < 650°C and 15 kbar < P < 26 kbar; ~60km) in an already cooled subduction system. The exhumation of these medium- and high-pressure rocks towards the shallow schistose serpentinites would have occurred either by discrete shear zones or inside sheath fold heads. All the ultramafic rocks of La Cabaña were then incorporated inside the accretionary prism, following the deformation style of D₁ near the base of the prism. Since then, they shared the same evolution as the enclosing metasediments, recording the subvertical D₂ shortening during uplift processes within the accretionary system and, later, the subhorizontal E-W D₃ shortening in more superficial conditions.

ACKNOWLEDGEMENTS

The editors of *Lithos* are thanked for the final editing of this paper. Anonymous referees are also thanked for their constructive review of the paper. This work was supported by Fondecyt Iniciación Grants (#11150635 and #11140005), and the RYC-2015-17596 to José María González-Jiménez. We also acknowledge Laurent Lenta (University of Nantes) and Jesús Montes-Rueda (University of Granada) for their careful preparation of thin sections, Philippe De Parseval and Sophie Gouy (Centre de Microcaractérisation Raimond Castaing) for assistance of EMPA work, Yann Morizet

(University of Nantes) for assistance during Raman analyses, Ricardo Silva for SEM analyses (UCh) and Loreto Troncoso for DRX assistance (UCh).

ACCEPTED MANUSCRIPT

REFERENCES:

- Agard, P., Yamato, P., Jolivet, L., Burov, E., 2009. Exhumation of oceanic blueschists and eclogites in subduction zones: Timing and mechanisms. *Earth-Science Reviews* 92(1–2), 53–79. doi:10.1016/j.earscirev.2008.11.002
- Alfaro, G., and Collao, S., 1990. Massive Sulfides in the Greenstone Belt of South-Central Chile – An Overview, *in* Fontbotè, L., Amstutz, G.C., Cardozo, M., Cedillo, E., and Frutos, J. eds., *Stratabound Ore Deposits in the Andes*: Berlin, Springer, p. 199–208.
- Amiguet, E., Van De Moortèle, B., Cordier, P., Hilairret, N., Reynard, B., 2014. Deformation mechanisms and rheology of serpentines in experiments and in nature. *Journal of Geophysical Research: Solid Earth* 119, 2013JB010791. DOI: 10.1002/2013JB010791
- Angiboust, S., Agard, P., Raimbourg, H., Yamato, P. & Huet, B. (2011). Subduction interface processes recorded by eclogite-facies shear zones (Monviso, W. Alps). *Lithos* 127(1), 222-238. doi:10.1016/j.lithos.2011.09.004
- Angiboust, S., Wolf, S., Burov, E., Agard, P., Yamato, P., 2012. Effect of fluid circulation on subduction interface tectonic processes: Insights from thermo-mechanical numerical modelling. *Earth and Planetary Science Letters* 357–358, 238–248. doi:10.1016/j.epsl.2012.09.012
- Arai, S., Ishimaru, S., 2007. Insights into Petrological Characteristics of the Lithosphere of Mantle Wedge beneath Arcs through Peridotite Xenoliths: a Review. *Journal of Petrology* 49(4), 665–695. doi:10.1093/petrology/egm069
- Barnes, J. D., Eldam, R., Lee, C.-T. A., Errico, J. C., Loewy, S., Cisneros, M., 2013. Petrogenesis of serpentinites from the Franciscan Complex, western California, USA. *Lithos* 178, 143–157. doi:10.1016/j.lithos.2012.12.018
- Barra, F., Gervilla, F., Hernández, E., Reich, M., Padrón-Navarta, J. A., González-Jiménez, J. M., 2014. Alteration patterns of chromian spinels from La Cabaña peridotite, south-central Chile. *Mineralogy and Petrology* 108(6), 819–836. doi:10.1007/s00710-014-0335-5
- Bebout, G. E., Penniston-Dorland, S. C., 2016. Fluid and mass transfer at subduction interfaces—The field metamorphic record. *Lithos* 240–243, 228–258. doi:10.1016/j.lithos.2015.10.007
- Blanco-Quintero, I.F., Proenza, J.A., Garcia-Casco, A., Tauler, E., Galí, S. 2011. Serpentinites and serpentinites within a fossil subduction channel: La Corea mélange, eastern Cuba. *Geologica Acta*, 9 (2-3), 1-17. doi:10.1344/105.000001662
- Cannaò, E., Scambelluri, M., Agostini, S., Tonarini, S., Godard, M., 2016. Linking serpentinite geochemistry with tectonic evolution at the subduction plate-interface: The Voltri Massif case study (Ligurian Western Alps, Italy), *Geochimica et Cosmochimica Acta*, 190, 115-133. doi: <http://dx.doi.org/10.1016/j.gca.2016.06.034>

Cardozo, N., Allmendinger, R. W., 2013. Spherical projections with OSXStereonet. *Computers & Geosciences* 51, 193–205. doi:10.1016/j.cageo.2012.07.021

Cloos, M., Shreve, R. L., 1988. Subduction-channel model of prism accretion, melange formation, sediment subduction, and subduction erosion at convergent plate margins: 2. Implications and discussion. *Pure and Applied Geophysics PAGEOPH* 128(3–4), 501–545. doi:10.1007/BF00874549

Colás, V., Padrón-Navarta, J. A., González-Jiménez, J. M., Fanlo, I., López Sánchez-Vizcaíno, V., Gervilla, F., Castroviejo, R., 2017. The role of silica in the hydrous metamorphism of chromite. *Ore Geology Reviews* 90, 274–286. doi:10.1016/j.oregeorev.2017.02.025

Connolly, J. A. D., 2009) The geodynamic equation of state: What and how: geodynamic equation of state-what and how. *Geochemistry, Geophysics, Geosystems* 10(10), n/a-n/a. doi:10.1029/2009GC002540

De Hoog, J. C. M., Hattori, K., Jung, H., 2014) Titanium- and water-rich metamorphic olivine in high-pressure serpentinites from the Voltri Massif (Ligurian Alps, Italy): evidence for deep subduction of high-field strength and fluid-mobile elements. *Contributions to Mineralogy and Petrology* 167(3). doi:10.1007/s00410-014-0990-x

Deschamps, F., Godard, M., Guillot, S., Hattori, K., 2013. Geochemistry of subduction zone serpentinites: A review. *Lithos* 178, 96–127. doi:10.1016/j.lithos.2013.05.019

Dick, H. J. B., Bullen, T., 1984. Chromian spinel as a petrogenetic indicator in abyssal and alpine-type peridotites and spatially associated lavas. *Contributions to Mineralogy and Petrology* 86(1), 54–76. doi:10.1007/BF00373711

Droop, G.T.R., 1987. A general equation for estimating Fe³⁺ concentrations in ferromagnesian silicates and oxides from microprobe analyses, using stoichiometric criteria. *Mineralogical Magazine* 51, 431–435.

Duhart, P., McDonough, M., Muñoz, J., Martin, M., Villeneuve, M., 2001. El Complejo Metamórfico Bahía Mansa en la cordillera de la Costa del centro-sur de Chile (39°30'–42°00'S): geocronología K-Ar, 40Ar/39Ar y U-Pb e implicancias en la evolución del margen sur-occidental de Gondwana. *Revista Geológica de Chile* 28(2). doi:10.4067/S0716-02082001000200003

Evans, B. W., 2004. The Serpentine Multisystem Revisited: Chrysotile Is Metastable. *International Geology Review* 46(6), 479–506. doi:10.2747/0020-6814.46.6.479

Evans, B.W., Dyar, M.D., Kuehner, S.M., 2012. Implications of ferrous and ferric iron in antigorite. *Am. Mineral.* 97, 184–196. DOI: doi:10.2138/am.2012.3926

Evans, K. A., Powell, R., Frost, B. R., 2013. Using equilibrium thermodynamics in the study of metasomatic alteration, illustrated by an application to serpentinites. *Lithos* 168–169, 67–84. doi:10.1016/j.lithos.2013.01.016

Federico, L., Crispini, L., Scambelluri, M., & Capponi, G. (2007). Ophiolite mélange zone records exhumation in a fossil subduction channel. *Geology*, 35(6), 499-502. doi: 10.1130/G23190A.1

Franzolin, E., Schmidt, M.W., Poli, S. (2011) Ternary Ca–Fe–Mg carbonates: subsolidus phase relations at 3.5 GPa and a thermodynamic solid solution model including order/disorder. *Contributions to Mineralogy and Petrology*, 161, 213–227. DOI 10.1007/s00410-010-0527-x

Frost, B.R., Beard J. S., 2007. On Silica Activity and Serpentinization. *Journal of Petrology* 48, 1351-1368. doi:10.1093/petrology/egm021

Gervilla, F., Padrón-Navarta, J. A., Kerestedjian, T., Sergeeva, I., González-Jiménez, J. M., Fanlo, I., 2012. Formation of ferrian chromite in podiform chromitites from the Golyamo Kamenyane serpentinite, Eastern Rhodopes, SE Bulgaria: a two-stage process. *Contributions to Mineralogy and Petrology* 164(4), 643–657. doi:10.1007/s00410-012-0763-3

Gerya, T. V., Stöckhert, B., Perchuk, A. L., 2002. Exhumation of high-pressure metamorphic rocks in a subduction channel: A numerical simulation: exhumation of high-pressure rocks. *Tectonics* 21(6), 6-1-6–19. doi:10.1029/2002TC001406

Glodny, J., Lohrmann, J., Echtler, H., Gräfe, K., Seifert, W., Collao, S., Figueroa, O., 2005. Internal dynamics of a paleoaccretionary wedge: insights from combined isotope tectonochronology and sandbox modelling of the South-Central Chilean forearc. *Earth and Planetary Science Letters* 231(1–2), 23–39. doi:10.1016/j.epsl.2004.12.014

González-Jiménez, J. M., Barra, F., Garrido, L. N. F., Reich, M., Satsukawa, T., Romero, R., Morata, D., 2016. A secondary precious and base metal mineralization in chromitites linked to the development of a Paleozoic accretionary complex in Central Chile. *Ore Geology Reviews* 78, 14–40. doi:10.1016/j.oregeorev.2016.02.017

González-Jiménez, J. M., Barra, F., Walker, R. J., Reich, M., Gervilla, F., 2014a. Geodynamic implications of ophiolitic chromitites in the La Cabaña ultramafic bodies, Central Chile. *International Geology Review* 56(12), 1466–1483. doi:10.1080/00206814.2014.947334

González-Jiménez, J. M., Griffin, W. L., Proenza, J. A., Gervilla, F., O'Reilly, S. Y., Akbulut, M., Arai, S., 2014b. Chromitites in ophiolites: How, where, when, why? Part II. The crystallization of chromitites. *Lithos* 189, 140–158. doi:10.1016/j.lithos.2013.09.008

González-Jiménez, J.M., Plissart, G., Garrido, L.N., Padrón-Navarta, J.A., Aiglsperger, T., Romero, R., Marchesi, C., Moreno-Abril, A. J., Reich, M., Barra, F., Morata D., 2017. Ti-clinohumite and Ti-chondrodite in antigorite serpentinites from Central Chile: evidence for deep and cold subduction. *European Journal of Mineralogy* 29(6), 959-970. DOI: 10.1127/ejm/2017/0029-2668.

Groppo, C., Rinaudo, C., Cairo, S., Gastaldi, D., Compagnoni R., 2006. Micro-Raman spectroscopy for a quick and reliable identification of serpentine minerals from

ultramafics. *European Journal of Mineralogy* 18, 319-329. DOI: 10.1127/0935-1221/2006/0018-0319

Guillot, S., Hattori, K., 2013. Serpentinites: Essential Roles in Geodynamics, Arc Volcanism, Sustainable Development, and the Origin of Life. *Elements* 9(2), 95–98. doi:10.2113/gselements.9.2.95

Guillot, S., Hattori, K. H., de Sigoyer, J., Nägler, T., Auzende, A.-L., 2001. Evidence of hydration of the mantle wedge and its role in the exhumation of eclogites. *Earth and Planetary Science Letters* 193(1–2), 115–127. doi:10.1016/S0012-821X(01)00490-3

Guillot, S., Hattori, K., Agard, P., Schwartz, S., Vidal, O., 2009. Exhumation processes in oceanic and continental subduction contexts: a review. In: Lallemand, S., Funicello F. (eds.). “Subduction Zone Dynamics”. Springer-Verlag Berlin Heidelberg, 175-204. doi: 10.1007/978-3-540-87974-9.

Guillot, S., Schwartz, S., Reynard, B., Agard, P., Prigent, C., 2015. Tectonic significance of serpentinites. *Tectonophysics* 646, 1–19. doi:10.1016/j.tecto.2015.01.020

Hacker, B. R., Peacock, S. M., Abers, G. A., Holloway, S. D., 2003. Subduction factory 2. Are intermediate-depth earthquakes in subducting slabs linked to metamorphic dehydration reactions?: subduction zone earthquakes and dehydration. *Journal of Geophysical Research: Solid Earth* 108(B1). doi:10.1029/2001JB001129

Hermann, J., Müntener, O., Scambelluri, M., 2000. The importance of serpentinite mylonites for subduction and exhumation of oceanic crust. *Tectonophysics* 327(3–4), 225–238. doi:10.1016/S0040-1951(00)00171-2

Hervé, F., Munizaga, F., Parada, M.A., Brook, M., Pankhurst, R., Snelling, N., Drake, R., 1988. Granitoids of the Coast Range of central Chile: geochronology and geologic setting. *J. S. Am. Earth Sci.* 1, 185–194. [http://dx.doi.org/10.1016/0895-9811\(88\)90036-3](http://dx.doi.org/10.1016/0895-9811(88)90036-3).

Hervé, F., Calderón, M., Fanning, C. M., Pankhurst, R. J., Godoy, E., 2013. Provenance variations in the Late Paleozoic accretionary complex of central Chile as indicated by detrital zircons. *Gondwana Research* 23(3), 1122–1135. doi:10.1016/j.gr.2012.06.016

Hilaret, N., Reynard, B., Wang, Y.B., Daniel, I., Merkel, S., Nishiyama, N., Petitgirard, S., 2007. High-pressure creep of serpentine, interseismic deformation, and initiation of subduction. *Science* 318, 1910-1913. DOI: 10.1126/science.1148494

Höfer, C., Kraus, S., Miller, H., Alfaro, G., Barra, F., 2001. Chromite-bearing serpentinite bodies within an arc–backarc metamorphic complex near La Cabaña, south Chilean Coastal Cordillera. *Journal of South American Earth Sciences* 14(1), 113–126. doi:10.1016/S0895-9811(01)00011-6

Holland, T. J. B., Powell, R., 2004. An internally consistent thermodynamic data set for phases of petrological interest: an internally consistent thermodynamic data set.

Journal of Metamorphic Geology 16(3), 309–343. doi:10.1111/j.1525-1314.1998.00140.x

Hyndman, R. D., Peacock, S. M., 2003. Serpentinization of the forearc mantle. Earth and Planetary Science Letters 212(3–4), 417–432. doi:10.1016/S0012-821X(03)00263-2

Hyppolito, T., García-Casco, A., Juliani, C., Meira, V. T., Hall, C., 2014. Late Paleozoic onset of subduction and exhumation at the western margin of Gondwana (Chilena Terrane): Counterclockwise P–T paths and timing of metamorphism of deep-seated garnet–mica schist and amphibolite of Punta Sirena, Coastal Accretionary Complex, central Chile (34° S). Lithos 206–207, 409–434. doi:10.1016/j.lithos.2014.07.023

Jabaloy-Sánchez, A., Gómez-Pugnaire, M. T., Padrón-Navarta, J. A., López Sánchez-Vizcaíno, V., Garrido, C. J., 2015. Subduction- and exhumation-related structures preserved in metaserpentinites and associated metasediments from the Nevado-Filábride Complex (Betic Cordillera, SE Spain). Tectonophysics 644–645, 40–57. doi:10.1016/j.tecto.2014.12.022

Jones, N.W., 1969: Crystallographic nomenclature and twinning in the humite minerals. Am. Mineral. 54, 309–313.

Kato, T. T., Sharp, W. D., Godoy, E., 2008. Inception of a Devonian subduction zone along the southwestern Gondwana margin: 40 Ar– 39 Ar dating of eclogite–amphibolite assemblages in blueschist boulders from the Coastal Range of Chile (41°S). Canadian Journal of Earth Sciences 45(3), 337–351. doi:10.1139/E08-006

Li, X.-P., Rahn, M., Bucher, K., 2004. Serpentinites of the Zermatt-Saas ophiolite complex and their texture evolution: Zermatt serpentinites. Journal of Metamorphic Geology 22(3), 159–177. doi:10.1111/j.1525-1314.2004.00503.x

López Sánchez-Vizcaíno, V., Trommsdorff, V., Gómez-Pugnaire, M.T., Garrido, C.J., Müntener, O., Connolly, J.A.D., 2005. Petrology of titanian clinohumite and olivine at the high-pressure breakdown of antigorite serpentinite to chlorite harzburgite (Almirez Massif, S. Spain). Contrib. Mineral. Petrol. 149, 627–646. DOI:10.1007/s00410-005-0678-3

Manning, C. E., 1997. Coupled Reaction and Flow in Subduction Zones: Silica Metasomatism in the Mantle Wedge. In B. Jamtveit & B. W. D. Yardley (Eds.), Fluid Flow and Transport in Rocks (pp. 139–148). Dordrecht: Springer Netherlands. doi:10.1007/978-94-009-1533-6_8

Mellini, M., Trommsdorff, V., Compagnoni, R., 1987. Antigorite polysomatism: behaviour during progressive metamorphism. Contributions to Mineralogy and Petrology 97(2), 147–155. doi:10.1007/BF00371235

Moral, J.C., Plissart, G., González-Jiménez, J.M., Garrido, L., Monnier, C., Diot, H., Berger, G., 2018. Condiciones de presión y temperatura de anfibolitas en Loma de Guzmán, Sector La Cabaña, IX Región. Congreso Geológico Chileno, 15, Concepción, Chile, 18-23 November 2018, 926-928.

- Nagaya, T., Wallis, S. R., Kobayashi, H., Michibayashi, K., Mizukami, T., Seto, Y., Matsumoto, M., 2014. Dehydration breakdown of antigorite and the formation of B-type olivine CPO. *Earth and Planetary Science Letters* 387, 67–76. doi:10.1016/j.epsl.2013.11.025
- Nozaka, T., 2005. Metamorphic history of serpentinite mylonites from the Happo ultramafic complex, central Japan. *J. metamorphic Geol.* 23, 711–723. doi:10.1111/j.1525-1314.2005.00605.x
- Orellana, F., Barra, F., Morata, D., Reich, M., Gervilla, F., Salazar, E., Romero, R., 2015. Origen de Cuerpos Máficos de la Serie Occidental del Basamento Metamórfico del Sur de Chile entre los 39°S y 40°S. Congreso Geológico Chileno, 14, La Serena, Chile, 4 - 8 Octubre 2015, 542-545.
- Padrón-Navarta, J.A., López Sánchez-Vizcaíno, V., Garrido, C.J., Gómez-Pugnaire, M.T., 2011. Metamorphic Record of High-pressure Dehydration of Antigorite Serpentinite to Chlorite Harzburgite in a Subduction Setting (Cerro del Almirez, Nevado-Filábride Complex, Southern Spain). *J. Petrol.* 52, 2047-2078. doi:10.1093/petrology/egr039
- Padrón-Navarta, J. A., Sánchez-Vizcaíno, V. L., Hermann, J., Connolly, J. A. D., Garrido, C. J., Gómez-Pugnaire, M. T., Marchesi, C., 2013. Tschermak's substitution in antigorite and consequences for phase relations and water liberation in high-grade serpentinites. *Lithos* 178, 186–196. doi:10.1016/j.lithos.2013.02.001
- Penniston-Dorland, S. C., Kohn, M. J., Manning, C. E., 2015. The global range of subduction zone thermal structures from exhumed blueschists and eclogites: Rocks are hotter than models. *Earth and Planetary Science Letters* 428, 243–254. doi:10.1016/j.epsl.2015.07.031
- Plissart, G., Bascuñán, L., Helle, T., Oyarzun, N., Soto, C., 2015. Accretionary prism mechanisms preserved in the Valdivia Coast basement (39°40'-39°53'S). Congreso Geológico Chileno, 14, La Serena, Chile, 4 - 8 Octubre 2015, 202-205.
- Pouchou, J.L. Pichoir, F., 1991. Quantitative analysis of homogeneous or stratified microvolumes applying the model "PAP". In: *Electron Probe Quantification* (eds Heinrich, K.J.F. & Newbury, D.E.), pp. 31–75. Plenum Press, New York.
- Powell, R. Holland, T. (1999) Relating formulations of the thermodynamics of mineral solid solutions: Activity modeling of pyroxenes, amphiboles, and micas. *American Mineralogist*, 84, 1–14. doi:10.2138/am-1999-1-201
- Rebay, G., Spalla, M. I., Zanoni, D., 2012. Interaction of deformation and metamorphism during subduction and exhumation of hydrated oceanic mantle: Insights from the Western Alps: deformation-metamorphism of HP serpentinites. *Journal of Metamorphic Geology* 30(7), 687–702. doi:10.1111/j.1525-1314.2012.00990.x
- Richter, P. P., Ring, U., Willner, A. P., Leiss, B., 2007. Structural contacts in subduction complexes and their tectonic significance: the Late Palaeozoic coastal

accretionary wedge of central Chile. *Journal of the Geological Society* 164(1), 203–214. doi:10.1144/0016-76492005-181

Romero, R., González-Jiménez, J.M., Barra, F., Leisen, M., Garrido, L.N., Talavera, C., Gain, S. E. M., Griffin, W. L., O'Reilly, S. Y., Reich M., Morata, D., 2017. Timing the tectonic mingling of ultramafic rocks and metasediments in the southern section of the coastal accretionary complex of central Chile. *International Geology Review*. doi:10.1080/00206814.2017.1402377

Scambelluri, M., Hoogerduijn Strating, E.H., Piccardo, G.B., Vissers, R.L.M., Rampone, E., 1991. Alpine olivine- and titanian clinohumite-bearing assemblages in the Erro-Tobbio peridotite (Voltri Massif, NW Italy). *J. Metamorph. Geol.* 9, 79-91. DOI: 10.1111/j.1525-1314.1991.tb00505.x

Scambelluri, M., Rampone, E., Piccardo, G.B., 2001. Fluid and element cycling in subducted serpentinite: a trace-element study of the Erro–Tobbio high pressure ultramafites (Western Alps, NW Italy). *Journal of Petrology* 42 (1), 55–67. doi:10.1093/petrology/42.1.55

Schwartz, S., Allemand, P., Guillot, S., 2001. Numerical model of the effect of serpentinites on the exhumation of eclogitic rocks: insights from the Monviso ophiolitic massif (Western Alps). *Tectonophysics* 342(1–2), 193–206. doi:10.1016/S0040-1951(01)00162-7

Schwartz, S., Guillot, S., Reynard, B., Lafay, R., Debret, B., Nicollet, C., Auzende, A. L., 2013. Pressure–temperature estimates of the lizardite/antigorite transition in high pressure serpentinites. *Lithos* 178, 197–210. doi:10.1016/j.lithos.2012.11.023

Shen, T., Hermann, J., Zhang, L., Lü, Z., Padrón-Navarta, J. A., Xia, B., Bader, T., 2015. UHP Metamorphism Documented in Ti-chondrodite- and Ti-clinohumite-bearing Serpentinized Ultramafic Rocks from Chinese Southwestern Tianshan. *Journal of Petrology* 56(7), 1425–1458. doi:10.1093/petrology/egv042

Trommsdorff, V., López Sánchez-Vizcaíno, V.L., Gómez-Pugnaire, M.T., Müntener, O., 1998. High pressure breakdown of antigorite to spinifex-textured olivine and orthopyroxene, SE Spain. *Contrib. Mineral. Petrol.* 132, 139-148. DOI: 10.1007/s004100050412

Whitney, D.L., Evans, B.W., 2010. Abbreviations for names of rock-forming minerals. *American Mineralogist* 95, 185–187. DOI: 10.2138/am.2010.3371

Willner, A. P., 2005. Pressure-Temperature Evolution of a Late Palaeozoic Paired Metamorphic Belt in North-Central Chile (34 -35 30'S). *Journal of Petrology* 46(9), 1805–1833. doi:10.1093/petrology/egi035

Willner, A. P., Thomson, S. N., Kröner, A., Wartho, J.-A., Wijbrans, J. R., Hervé, F., 2005. Time Markers for the Evolution and Exhumation History of a Late Palaeozoic Paired Metamorphic Belt in North-Central Chile (34 -35 30'S). *Journal of Petrology* 46(9), 1835–1858. doi:10.1093/petrology/egi036

SUPPORTING INFORMATION:

Appendix S1. Field observations and characteristic microstructures in the micaschists surrounding the La Cabaña ultramafic massif.

Appendix S2. Major and minor elements analyses of representative lithotypes.

Appendix S3. XRD patterns of representative lithotypes for La Cabaña.

Appendix S4. Representative microprobe analyses of silicates, spinels and carbonates.

Appendix S5. Micro-Raman spectroscopy on serpentines.

Appendix S6. Methods of calculations of effective compositions during metamorphic peak for pseudosection construction

FIGURES CAPTIONS:

Figure 1. (a) Geological setting and location of the study area in the Western Series (modified from Hervé et al., 2013). (b) Geological map of the La Cabaña area modified from Höfer et al. (2001), with the different ultramafic bodies, the location of the good outcrop exposures in the Centinela Bajo Norte massif and the representative S_2 foliation in micaschists and ultramafic rocks (this study).

Figure 2. Structural maps of the Centinela Bajo Norte good exposures, displaying the three recognized ductile deformation phases in the ultramafic rocks.

Figure 3. Structural measurements associated to the four recognized deformation phases in the La Cabaña area, represented in stereographic equal area projections. Max. eigenvectors and contour plots (C.I.: 2% / 1% area) have been determined using the Stereonet software developed by R. W. Allmendinger (Cardozo and Allmendinger, 2013).

Figure 4. Field observations of the deformation phases inside the ultramafic rocks, D₁ (a-e), D₂ (f-i), D₃ (j-k). (a) Stretching lineation L1 in olivine-bearing mylonitic serpentinites, marked by alignment of olivine-magnetite lenses. (b) Rare top-to-the-east shear band in mylonitic serpentinite. (c) Stretching lineation L1 in mylonitic serpentinites, marked by antigorite preferred orientation. (d-e) Section of F₁ tubular fold made of partially serpentinized massive peridotites enclosed in schistose serpentinites. The small photography displays the development of antigorite foliation and crenulation at the lens borders. (e) Typical schistose serpentinites and associated S₂ dipping to the east. (d) Schistose serpentinites displaying recumbent crenulation of S₁ and development of new S₂ crenulation cleavage. (e) Influence of D₁ competent lenses on the orientation of S₂ cleavage in schistose serpentinites. (f) Folding of pyroxenitic vein with axial plane parallel to S₂. (g) S₃ crenulation cleavage in schistose serpentinites. (h) Metric upright F₃ in soap- white schistose serpentinites. Atg: antigorite; Ctl: chrysotile.

Figure 5. Simplified drawings of representative microstructures and assemblages of ultramafic rocks from the study area. (a) MP: Partially serpentinized massive peridotites. (b) LSch-MP: Locally schistose, partially serpentinized massive peridotites. (c) SchS: Schistose serpentinites. (d) Cren-SchS: Crenulated schistose serpentinites. (e) MyS: Mylonitic serpentinites. (f) Cren-MyS: Crenulated mylonitic serpentinites. (g) OMyS: Olivine-bearing serpentinites. (h) Cren-TiChu&OMyS: Crenulated Ti-clinohumite and olivine-bearing serpentinites. Mineral abbreviations (Whitney and Evans, 2010): Atg, antigorite; Ctl, chrysotile (Ctl D2: chrysotile associated to D2; Late Ctl: chrysotile crosscutting veins); Chr, chromite; Dol,

dolomite; Lz, lizardite; Mag, magnetite; Ol, olivine (Ol I: primary olivine; Ol II: metamorphic olivine); Ti-Chn, Ti-chondrodite; Ti-Chu, Ti-clinohumite.

Figure 6. Photomicrographs of characteristic microstructures of serpentinites from La Cabaña ultramafic massif. **(a) MP.** Lizardite mesh texture after primary olivine (Ol I) and crosscutting chrysotile vein (Late Ctl). **(b) MP.** Representative chromite rims (reflective light). **(c) LSch-MP.** Veinlet-like secondary antigorite in nascent foliation superimposing mesh texture near horizontal contact with schistose serpentinites, defining S_1 - S_2 . (See also hand-specimen Figure 4d1). **(d) LSch-MP.** Secondary antigorite foliation S_1 superimposing mesh texture and crenulated by D_2 near the vertical contact with schistose serpentinites (See also hand-specimen Fig. 4d2). Note chrysotile veinlet Ctl D_2 located in the F_2 limbs and subparallel to S_2 . **(e) Cren-SchS.** Static antigorite superimposing the lizardite mesh texture and dynamic antigorite in foliation S_1 , later crenulated by D_2 . Symmetric crenulation of S_1 and development of S_2 axial plane cleavage, characterized by thickened hinges and thinned limbs of the Lz-Ol I ribbons. Note Ctl D_2 veinlet. **(f) MyS.** Interpenetrating static Atg lens in a S_1 foliated matrix antigorite, displaying a top to the west. (Crossed polarizers light with inserted compensator). Note intergrowth between static Atg and magnetite in interpenetrating Atg lens. **(g) MyS.** Typical chromite rims (reflective light). Note the inclusions of Atg in the magnetite outer rim, which are absent in the chromite from MP and SchS. **(h) Cren-MyS.** Symmetric crenulation of S_1 and development of S_2 axial plane cleavage, generally erasing previous static Atg lenses. **(i) OMyS.** Lens of Ol II + Dol + Atg + Mag in a foliated S_1 antigorite. Ol II poikiloblast occurs as small grains in optical continuity englobing Atg needles inclusions and magnetite. **(j) OMyS.** Ribbon of Ol II + Dol + Mag in a foliated S_1 antigorite. Note the shape

preferred orientation of Ol II and magnetite grains. **(k) OMyS.** Details of ribbons displaying magnetite inclusions in Ol II and Dol, evidencing the metamorphic character of these minerals. Zoom in reflective light on Ol II inclusions inside magnetite and smooth contacts between Mag and Ol II. **(l) OMyS.** Typical chromite rims, similar as in MyS but with reduced core and developed outer Atg-Mag rim (reflective light). **(m) OMyS.** SEM microphotograph displaying dolomite, Ol II and Atg as inclusions inside magnetite. **(n) TiChu&OMyS.** Relationships between Ol II, Ti-Chu, Atg and Mag. Note the smooth contacts between Ol II and Ti-Chu (small-scale intergrowths). Antigorite needles are found as continued inclusions in TiChu, Ol II and Mag (arrows). Note magnetite inclusions in Ol and TiChu. **(o) TiChu&OMyS.** Crenulation of S_1 and development of S_2 axial plane cleavage, characterized by thickened hinges and thinned limbs of the Ol + TiChu + Mag + Atg \pm Ti-Chn ribbons. Note the presence of Ctl D2 veinlet. Mineral abbreviations as in Figure 5.

Figure 7. Compositional diagrams for the main silicate minerals observed in the ultramafic rocks from La Cabaña ultramafic massif. **(a)** Mn versus Fo contents in olivine. Note high Mn contents in OMyS and TiChu&OMyS indicating metamorphic origin. Fo contents seem mainly controlled by bulk rock composition (values of Mg# of 0.956 and 0.940 for OMyS and TiChu&OMyS, respectively) and possibly by partitioning coefficients with the associated mineralogical assemblage. **(b)** Mn and Fo contents core to rim profiles in olivine. Note that Fo contents increase towards rim in OMyS and TiChu-OMyS whereas Mn contents decrease in OMyS. **(c)** Al versus Si in antigorite. Note high Al contents in MP and increasing Al contents from SchS to MyS to TiChu&OMyS. **(d)** Ti versus metals diagram for Ti-clinohumite, Ti-humite and Ti-

chondrodite, showing the theoretical compositional vector $\text{TiO}_2\text{Mg}_{-1}\text{F}_{-2}$. We noted an inverse correlation between TiO_2 and SiO_2 , MgO or $\text{OH}(\text{calc.})$.

Figure 8. Compositional diagrams for chromites of the ultramafic rocks from La Cabaña massif. **(a)** Cr# [$\text{Cr}/(\text{Cr}+\text{Al})$ atomic ratio] versus Mg# [$\text{Mg}/(\text{Mg}+\text{Fe}^{2+})$ atomic ratio] diagram discriminating core, Fe^{2+} -rich porous, Fe^{3+} -rich homogeneous and magnetite rims in chromite grains from the different ultramafic lithotypes. Dashed lines in **(a)** denote the composition of olivine in equilibrium with chromite at a nominal temperature of 1200°C (Dick and Bullen, 1984). Cr-spinels from forearc peridotites from Arai and Ishimaru (2007). Chromite cores from La Cabaña Centinela Bajo Norte chromitites from González-Jiménez et al. (2016). **(b)** Ternary Al-Cr- Fe^{3+} diagram discriminating core and Fe^{2+} -rich porous, Fe^{3+} -rich homogeneous and magnetite rims in chromite grains from the different ultramafic lithotypes.

Figure 9. Chromite alteration stages and relationships with serpentine minerals. (i) to (iv) represent evolution from fresh dunite material to lizarditic meta-dunite during retrograde path and local prograde antigoritization. (i) and (ii) represent initial and Fe^{2+} porous rim chromite formation, respectively, and correspond to stages partially overprinted by (iii) formation of Fe^{3+} homogeneous chromite, magnetite and lizarditization and (iv) recrystallization of magnetite rims and antigoritization. (v) and (vi) represent prograde path between mylonitic antigoritite and olivine-bearing antigoritite. D_2 responsible for crenulation is not considered in this figure.

Figure 10. **(a)** PT diagram displaying stability fields of serpentine minerals (from Schwartz et al. 2013) and worldwide prograde subduction paths (from Penninston-

Dorland et al. 2015). The base of the Chilean paleo-accretionary prism, based on metamorphic peak registered in metasediments in the Western Series (Willner 2005), is showed for comparison. **(b)** Pseudosection calculated in the FMASH system with H₂O in excess for mylonitic serpentinite, displaying a large field for Atg + Tlc. Isopleths of $X_{Al}(Atg) = Al(apfu)/8$ (defined by Padrón-Navarta et al. 2013) are showed as dotted blue lines. Note that a minimum of $X_{Al}(Atg) = 0.095$ is observed in the pseudosection whereas interpenetrating and foliation blades display values of 0.082 and 0.079, respectively. **(c)** Pseudosection calculated in the FMASH system with H₂O in excess for olivine-bearing mylonitic serpentinite, displaying the field Atg + Ol. Isopleths of $X_{Al}(Atg)$ are showed as dotted blue lines, volume amounts of olivine as red lines, Fo contents as dotted yellow lines and volume amounts of brucite in dotted black lines. Field for Atg + Ol + Dol reproduced from (d) and star corresponding to intersection of (c) and (d). **(d)** Pseudosection calculated in the CFMASH system with H₂O-CO₂ ($X_{CO_2} = 0.02$) in excess for dolomite and olivine-bearing mylonitic serpentinite, displaying the field of Atg + Ol + Dol. The carbonate solid solution (Cb*) mainly consists of magnesite and siderite, with very low amounts of calcite (< 1%). Same isopleths color code as (c), volume amounts of dolomite in magenta lines.

Figure 11. Tectono-metamorphic evolution of La Cabaña ultramafic rocks in the paleo-subduction setting of South-Central Chile. Note the different evolutions between southern (opening of a back-arc basin) and northern parts. **(a)** Localization of dunites-harzburgites-chromitites in an incipient back-arc basin at 380-370 Ma. **(b)** Closure of the back-arc basin and arc subduction, leading to static hydration of the hanging wall (spinel alteration and lizarditization I). Formation of the mylonitic and

olivine-bearing mylonitic serpentinites at depths in the subduction channel. **(c)** Accretionary prism thickening. The former hanging wall is captured by the subduction channel, leading to partial antigoritization of the partially serpentinitized massive peridotites, which are now embedded in schistose serpentinites. Formation of Ti-clinohumite & olivine-bearing mylonitic serpentinites at depths in the subduction channel. **(d)** Exhumation of deep-seated serpentinites (MyS, OMyS and Ti-ChuOMyS) along the subduction channel and their incorporation inside the schistose serpentinites near the base of the accretionary prism. **(e)** Incorporation of all ultramafic rocks from the La Cabaña massif in the accretionary prism. Grey field: Limits of prograde worldwide oceanic subduction paths of Penniston-Dorland et al. (2015). Box of garnet-bearing amphibolites from nearby Loma Guzman from Moral et al. (2018). Field of Ti-Chu + Ti-Chn + Ol + Atg from Shen et al. (2015).

Figure 12. **(a)** 3D sketch showing where the La Cabaña ultramafic lithotypes formed and their incorporation inside the shallow serpentinitic channel, in a context of subduction channel and accretionary prism, between 0 and 80 km depth. View of the subduction channel architecture inspired from Angiboust et al. (2012). (Olivine-bearing) mylonitic serpentinites derived from the stagnant hanging wall whereas Ti-clinohumite & olivine-bearing mylonitic serpentinites exhumed from higher depths. D_1 corresponds to the deformation associated to the subduction channel (stretching perpendicular to the trench) and prevails at different temperatures (linked to different depths and/or different times in the evolution of the subduction system). At high depths, rheological contrasts are attenuated whereas in shallower parts, near the base of the accretionary prism, these phenomena are dominant and similar to those in the deepest parts of the prism. D_2 corresponds to a subvertical shortening inside the

accretionary prism, once the ultramafic rocks were already incorporated within the prism. D_3 is a subhorizontal E-W shortening occurring in more superficial conditions.

(b) Widening of the serpentinitic subduction channel at shallow depths. The partially statically lizarditized hanging mantle is progressively antigoritized, with high localization of fluids circulation and D_1 deformation, generating competent massive domains embedded in low-viscous schistose matrix.

ACCEPTED MANUSCRIPT

Highlights

- Shallow portions of the subduction channel can be captured in the accretionary prism.
- Hanging mantle lenses are dragged and tectonically mixed in the subduction channel.
- Medium and high-T serpentinites can exhume to shallow portions of the channel.
- Within-channel exhumation occurred in sheared zones or within the sheath folds head.
- Localized deformation and fluid pathways characterize shallow subduction channel.

ACCEPTED MANUSCRIPT

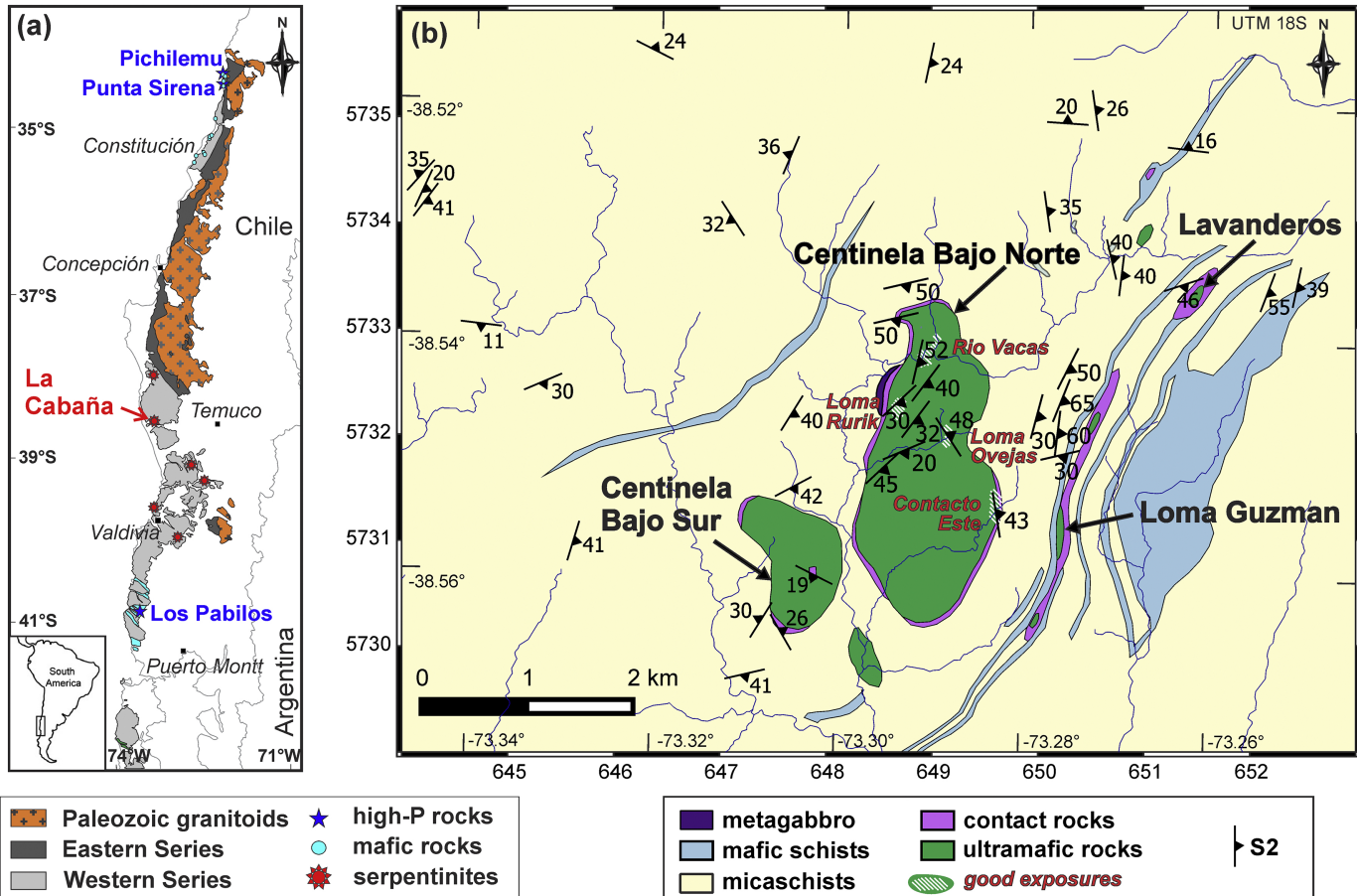


Figure 1

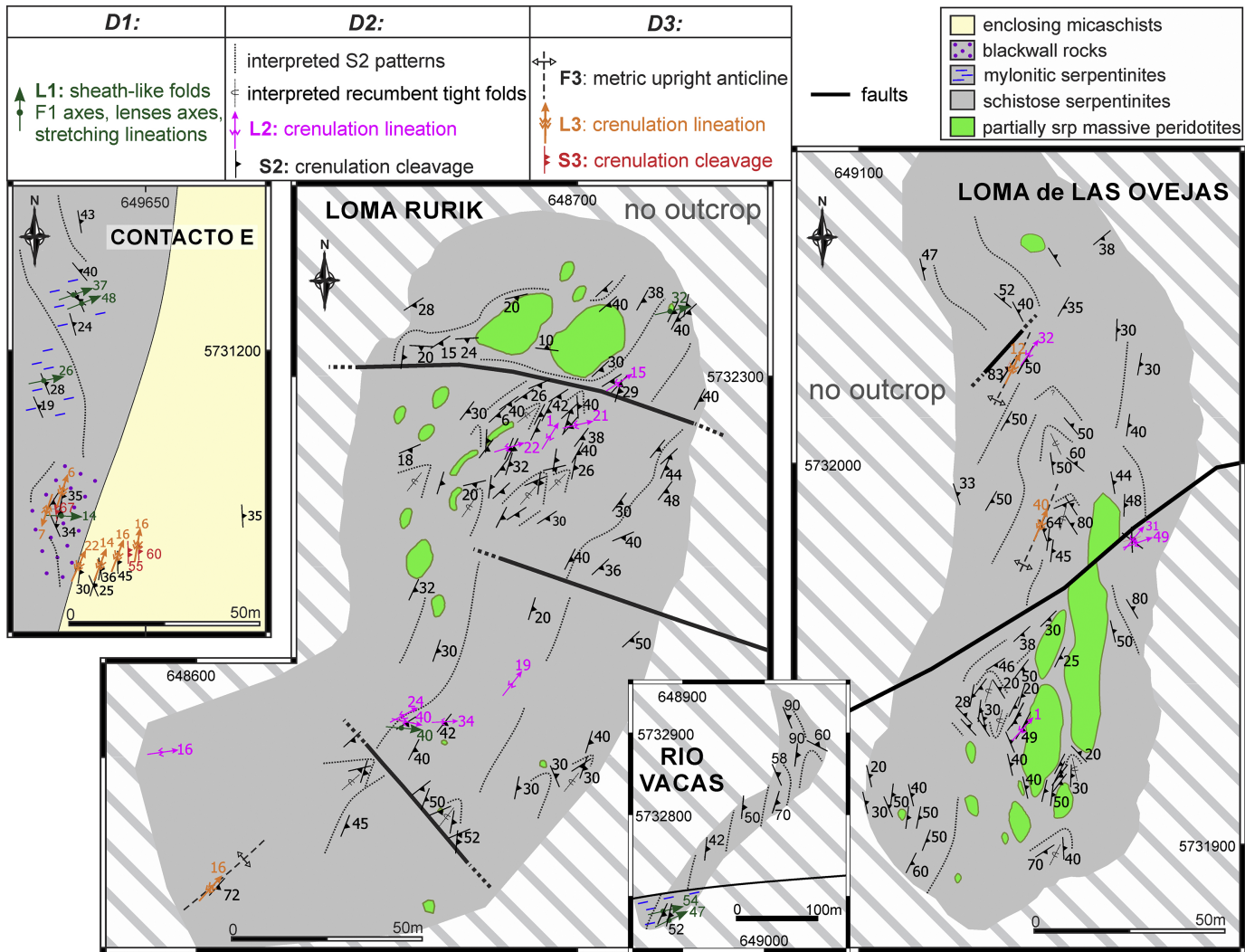
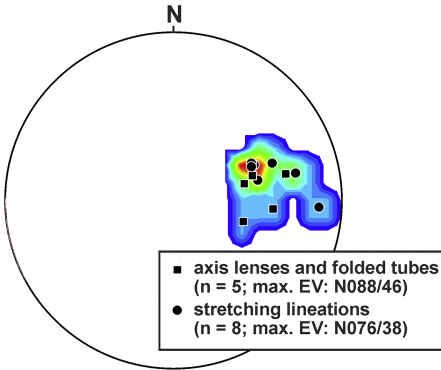


Figure 2

Ultramafic rocks

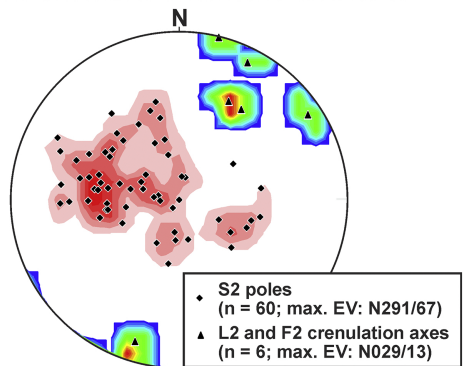
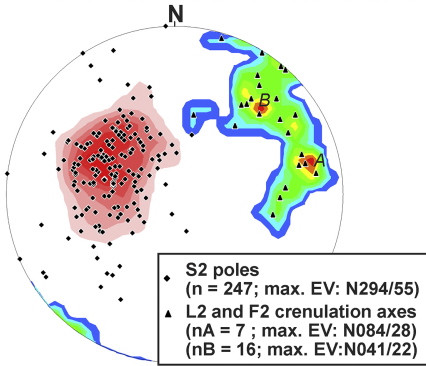
Enclosing micaschists

D1

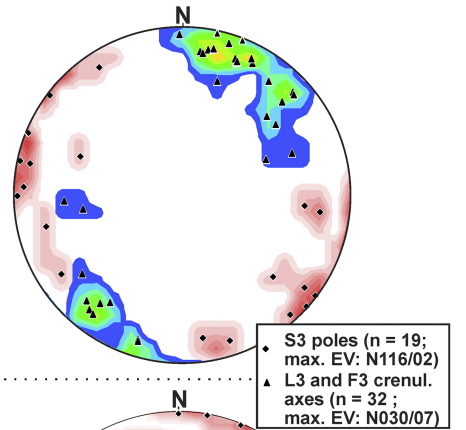
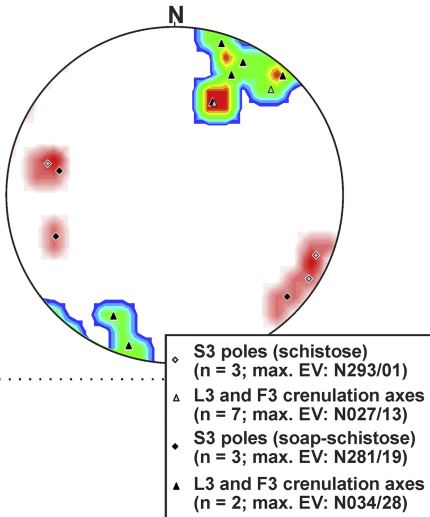


not observed

D2



D3



D4

not observed

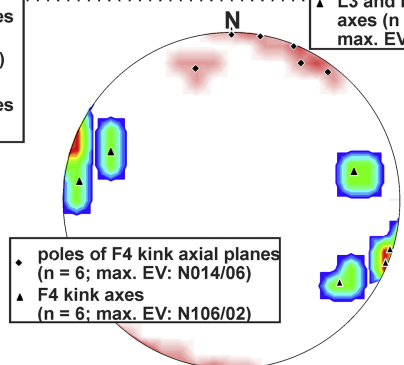


Figure 3

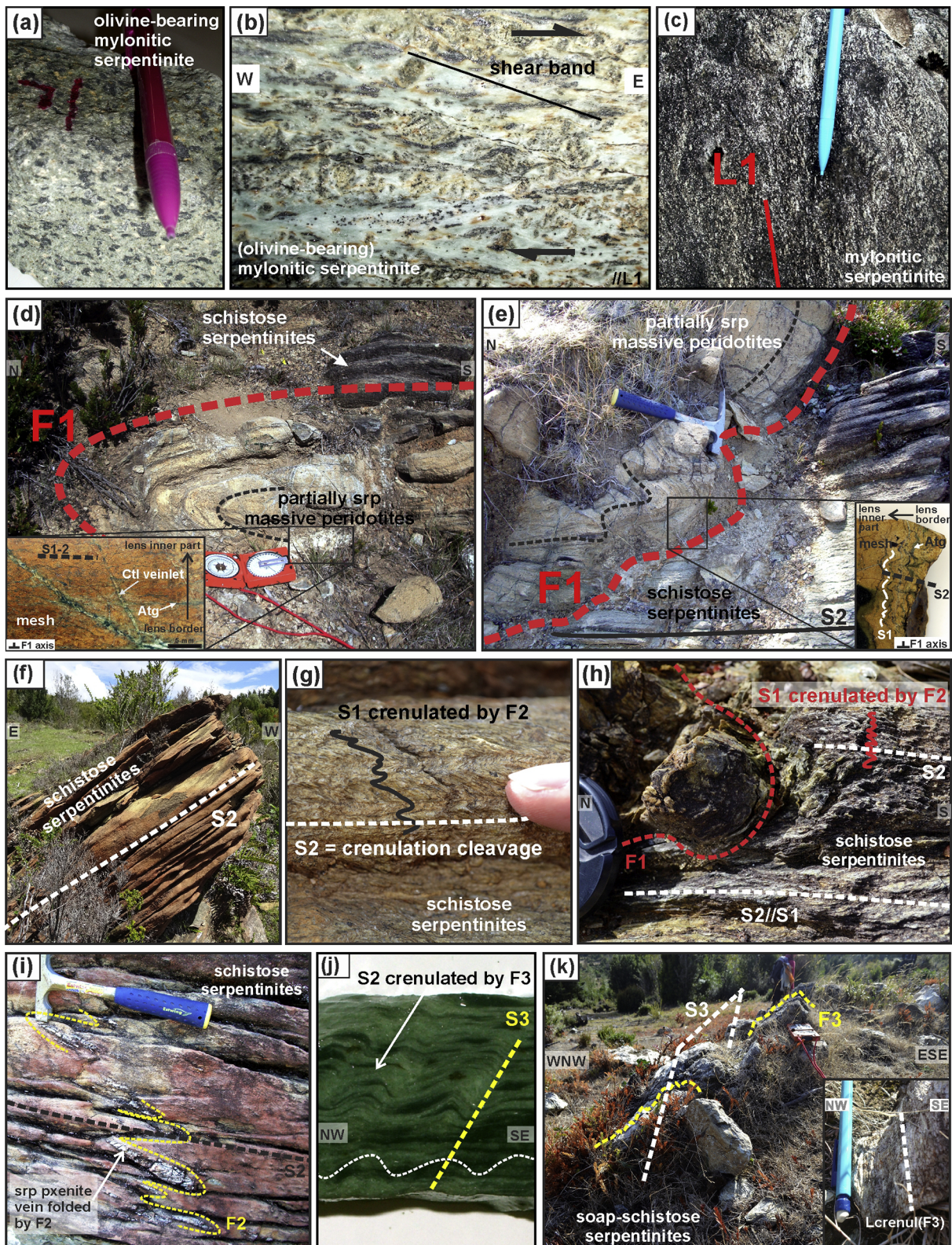


Figure 4

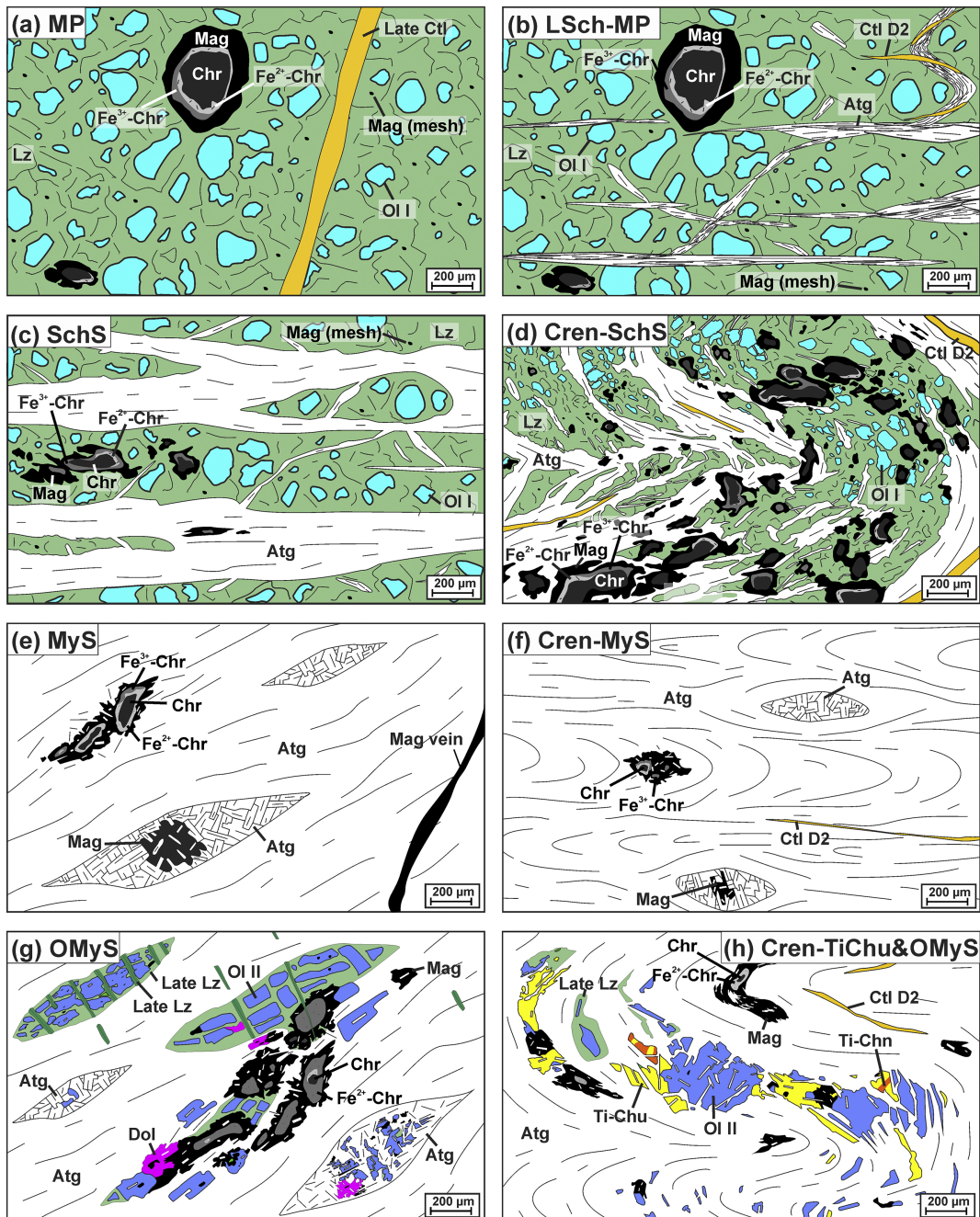


Figure 5

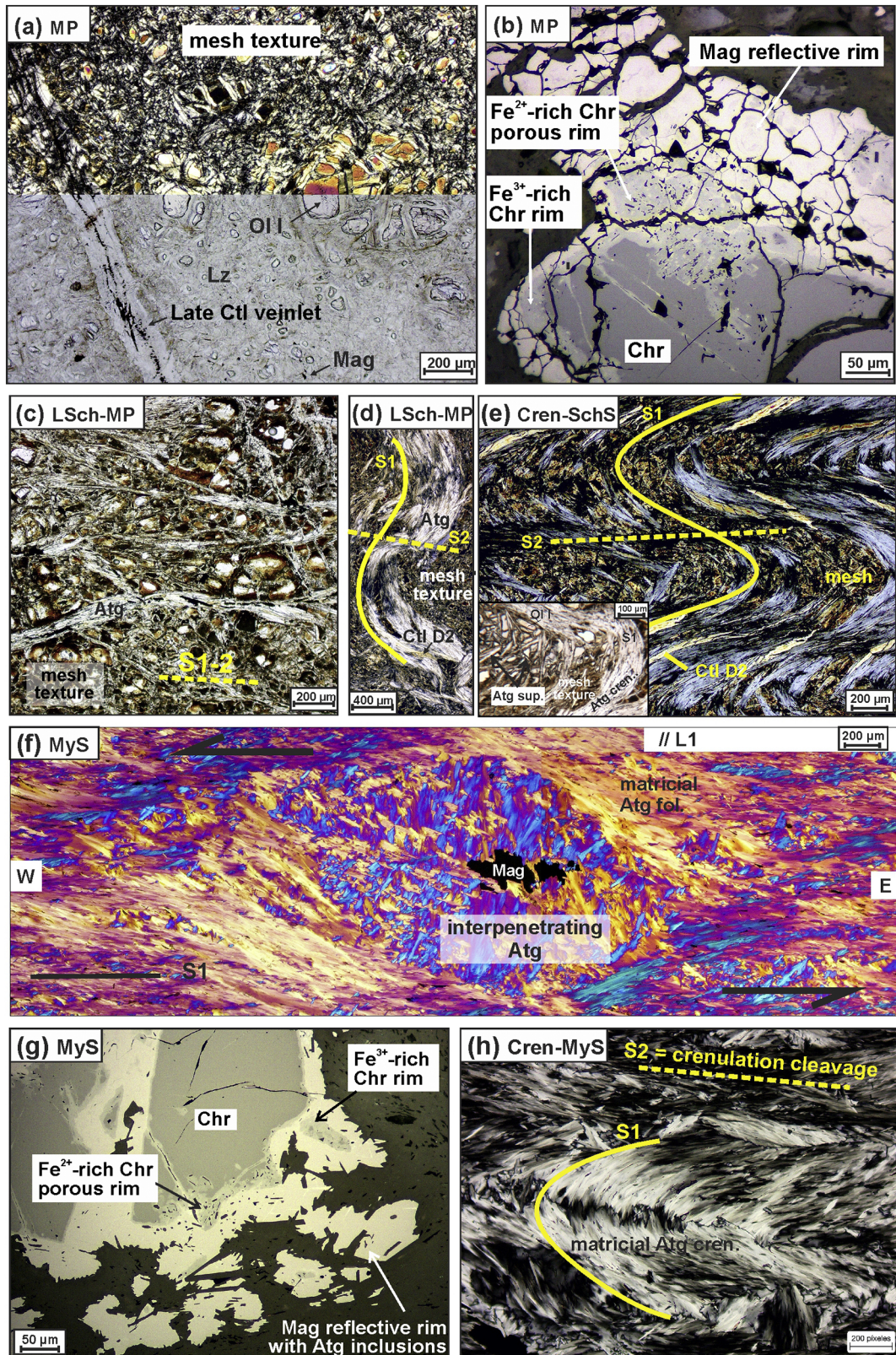


Figure 6A

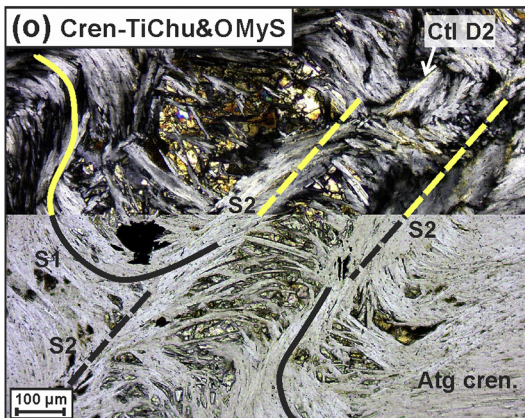
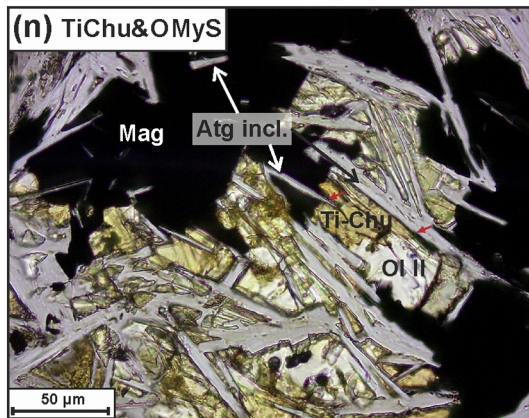
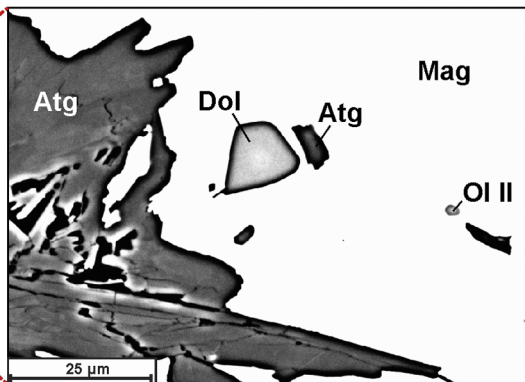
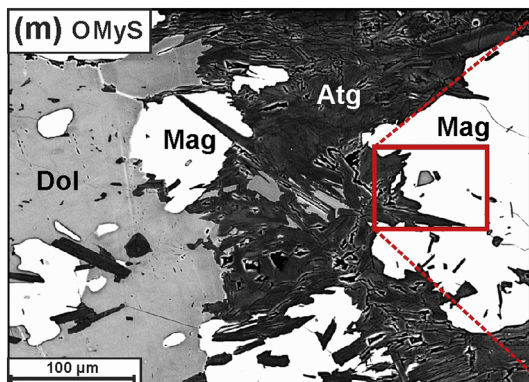
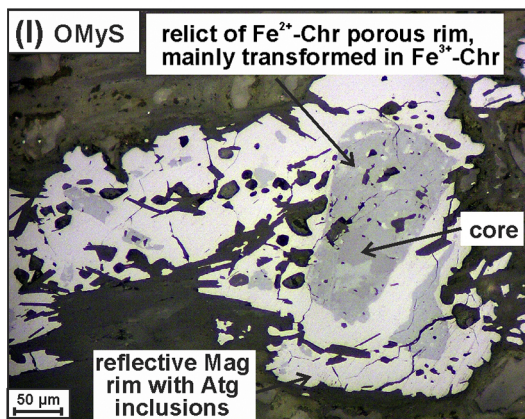
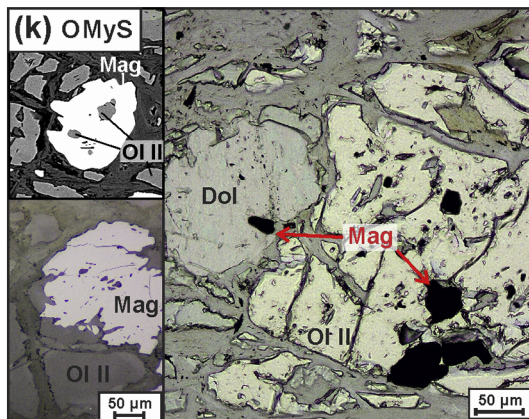
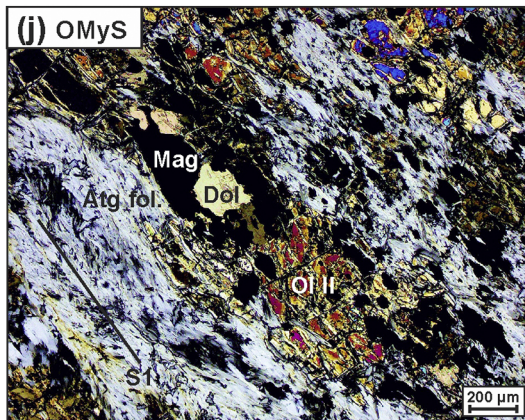
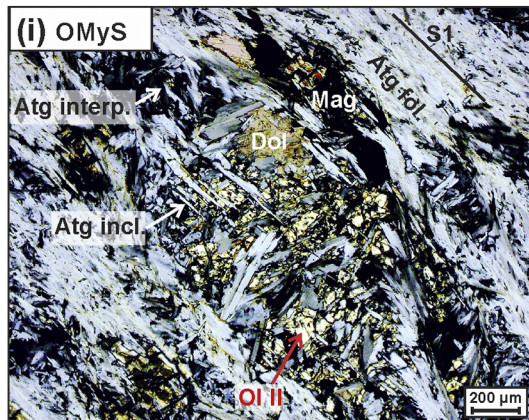


Figure 6B

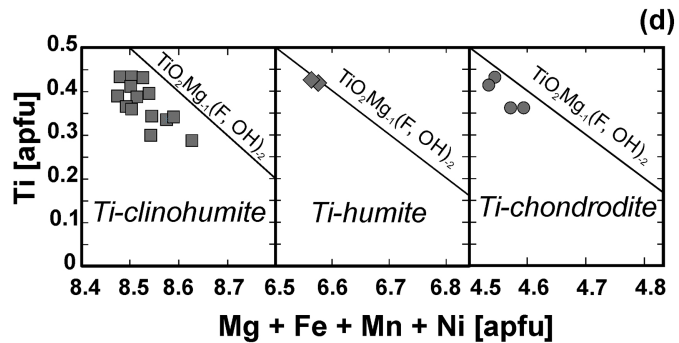
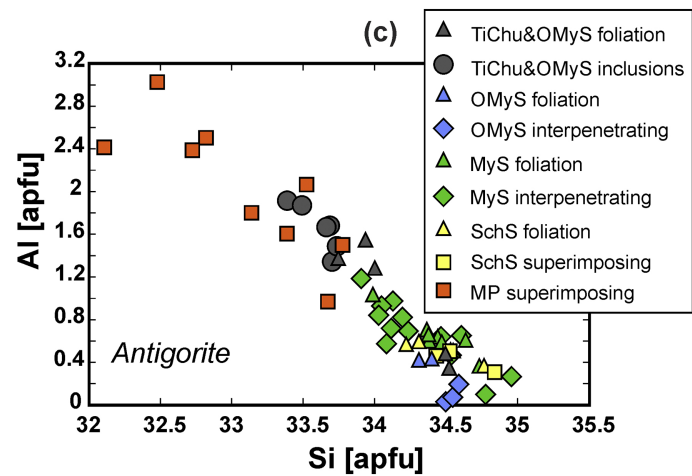
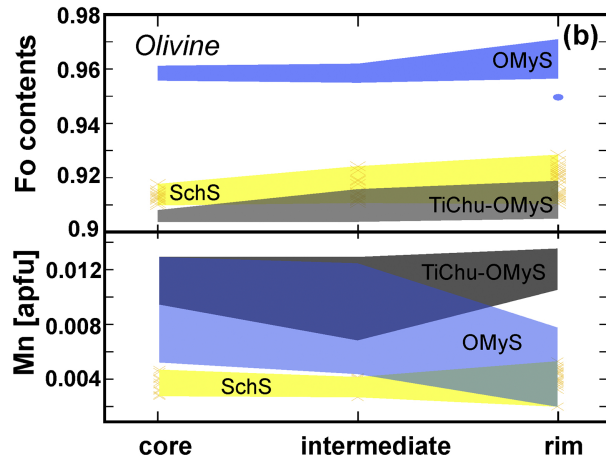
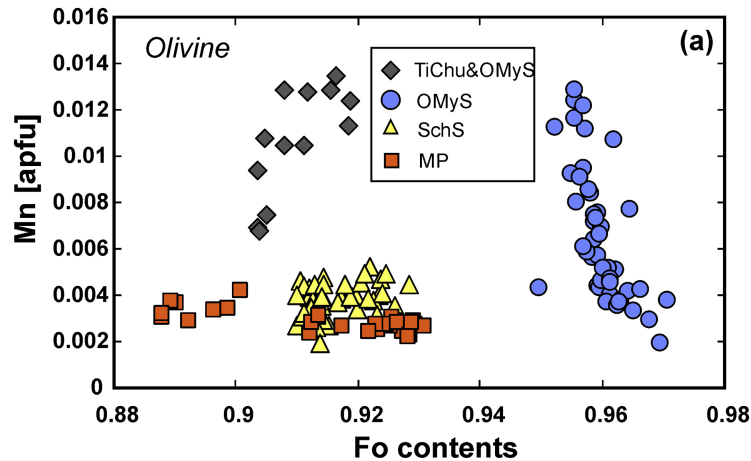


Figure 7

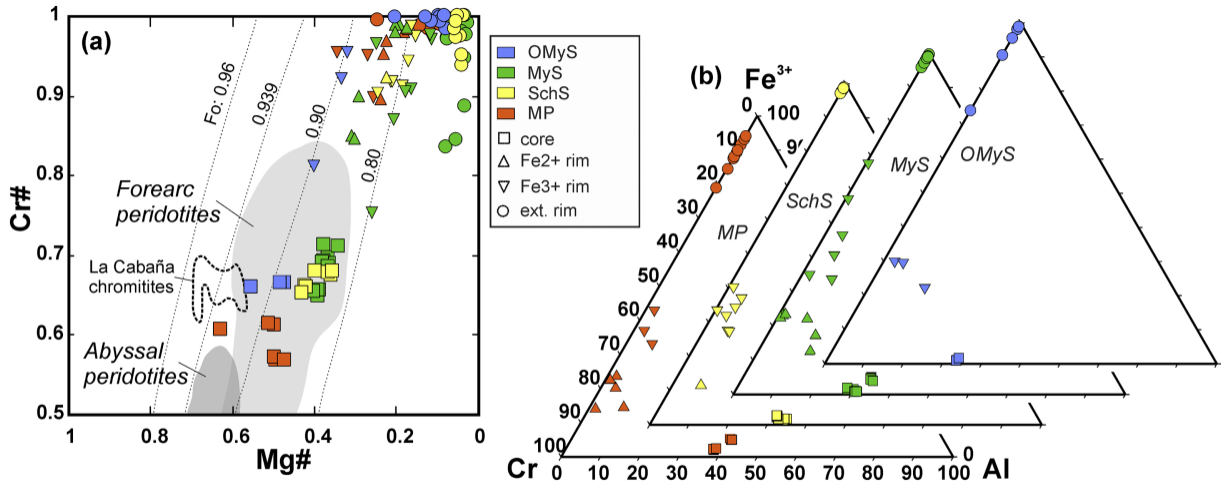


Figure 8

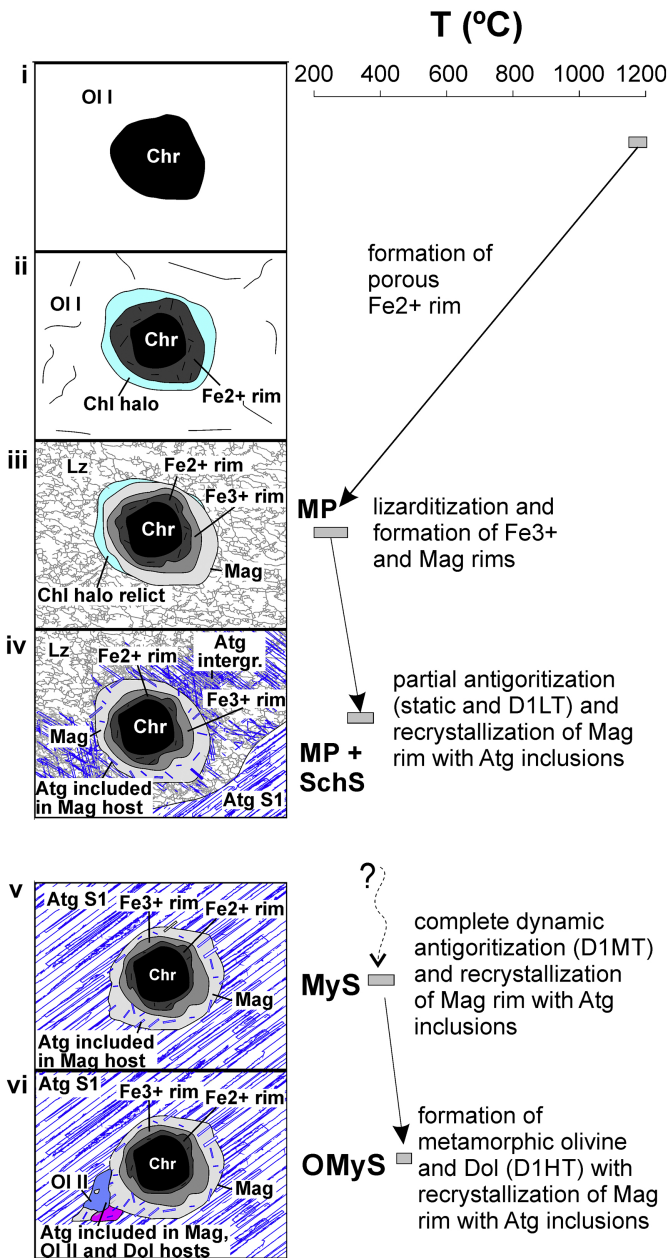


Figure 9

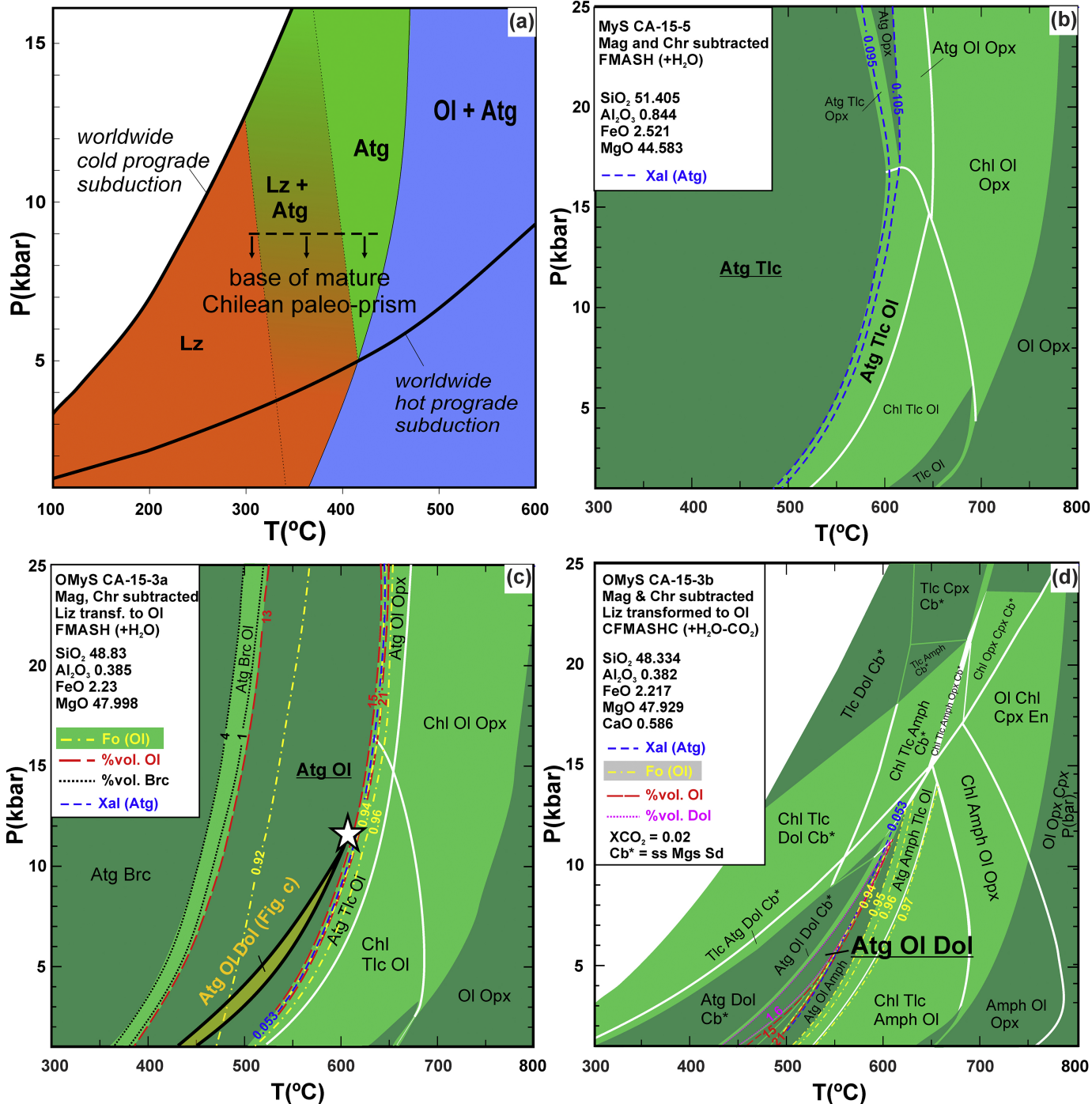


Figure 10

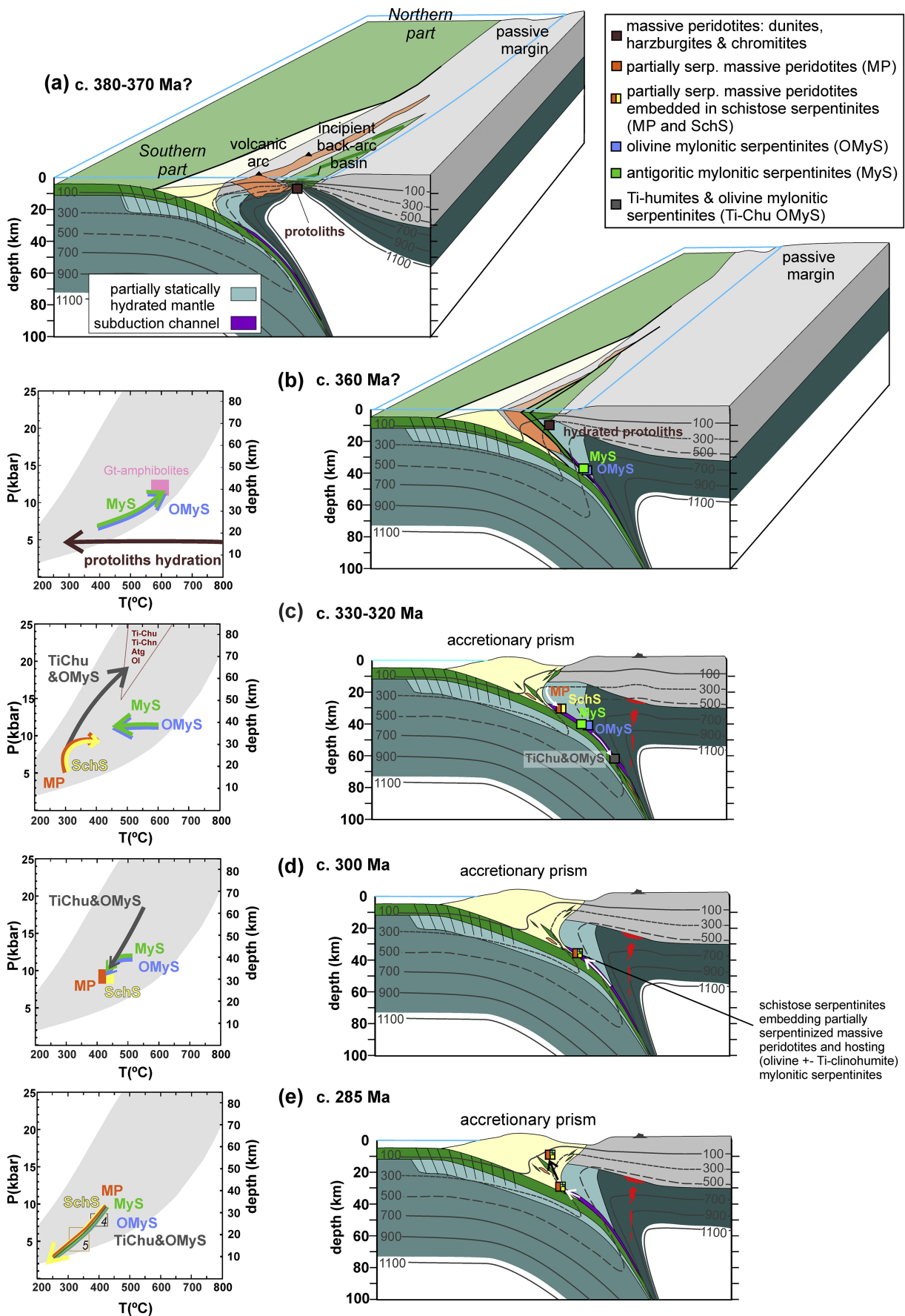


Figure 11

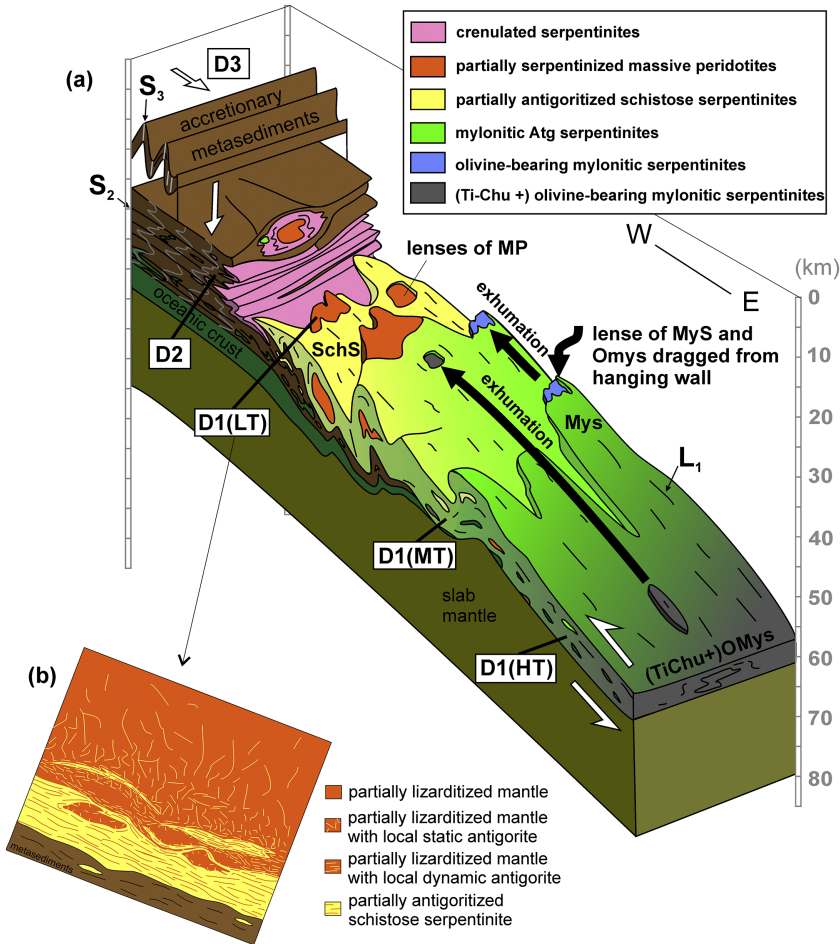


Figure 12